Received: 18 July 2022 | Revised: 14 October 2022 | Accepted: 20 October 2022

DOI: 10.1002/aoc.6942

RESEARCH ARTICLE

Applied Organometallic Chemistry WILEY

A detailed experimental and computational study of Cd complexes with pyridyl-based thiazolyl hydrazones

Sanja B. Kokanov[1] | **Nenad R. Filipović**[2] | **Aleksandar Višnjevac**[3] | **Milan Nikolić**[1] | **Irena Novaković**[4] | **Goran Janjić**[4] | **Berta Barta Holló**[5] | **Sandra Ramotowska**[6] | **Paulina Nowicka**[6] | **Mariusz Makowski**[6] | **Özlem Uğuz**[7] | **Atıf Koca**[7] | **Tamara R. Todorović**[1]

[1]University of Belgrade - Faculty of Chemistry, Studentski trg 12-16, Belgrade, 11000, Serbia

[2]University of Belgrade - Faculty of Agriculture, Nemanjina 6, Belgrade, 11000, Serbia

[3]Division of Physical Chemistry, Institute Ruđer Bošković, Bijenička Cesta 54, Zagreb, 10000, Croatia

[4]Institute of Chemistry, Technology and Metallurgy, University of Belgrade, Njegoševa 12, Belgrade, Serbia

[5]Department of Chemistry, Biochemistry and Environmental Protection, Faculty of Sciences, University of Novi Sad, Trg Dositeja Obradovića 3, Novi Sad, 21000, Serbia

[6]Faculty of Chemistry, University of Gdansk, PL80-308 Gdansk, Poland

[7]Engineering Faculty, Department of Chemical Engineering, Marmara University, 34722 Goztepe, Istanbul, Turkey

Correspondence
Tamara R. Todorović, University of Belgrade - Faculty of Chemistry, Studentski trg 12-16, 11000 Belgrade, Serbia.
Email: tamarat@chem.bg.ac.rs

Funding information
Ministry of Education, Science and Technological Development of the Republic of Serbia, Grant/Award Numbers: 451-03-68/2022-14/200026, 451-03-68/2022-14/200125, 451-03-68/2022-14/200116, 451-03-68/2022-14/200168; Turkish Academy of Sciences

Interest in Cd complexes has been growing in recent years. Cd complexes are considered a potential solution in the search for novel antibiotics that can fight antimicrobial resistance. In addition, Cd complexes draw attention to material chemistry. The main objective of this work was to prepare the first Cd(II) complexes with anionic forms of pyridine-based thiazolyl hydrazone (THs) ligands HLS^2 [(*E*)-4-(4-methoxyphenyl)-2-(2-[pyridine-2-ylmethylene] hydrazinyl)thiazole] and HLS^3 [(*E*)-2-(2-[pyridine-2-ylmethylene]hydrazinyl)-4-(p-tolyl)thiazole] and perform their structural and spectroscopic characterization, as well as stability in solution and upon heating. Studies related to their biological activities and possible electrochromic applications are also being conducted. Complexes $[Cd(HLS^2)_2]$ (**1**) and $[Cd(HLS^3)_2]$ (**2**) have been characterized by a single-crystal X-ray diffraction and computational analysis of intermolecular interactions responsible for their solid-state structures was performed. Thermal stability of **1** and **2** in the solid-state was analyzed by TGA/MS, where as their solution stability was determined by the spectrophotometric titration method. Electrochemical and *in situ* UV–Vis spectroelectrochemical analyses of **1** and **2** were carried out to determine redox mechanisms and the influence of the substituents and electrolytes on their redox responses. The antioxidant capacity of both complexes was tested in antioxidant assays, while their antimicrobial activity was tested against five Gram-positive and four Gram-negative bacteria, as well as against three fungi. The obtained results indicate their potent antioxidant capacity. The antimicrobial activity of investigated compounds on almost all tested bacterial strains was stronger than that of the standard antibiotic erythromycin. The results of docking studies indicate that the minor groove DNA is the possible biological target of **1** and **2**.

KEYWORDS
antimicrobial activity, Cd(II) complex, docking, *in situ* spectroelectrochemistry, thiazolyl hydrazones

1 | INTRODUCTION

Cadmium has been classified by the International Agency for Research on Cancer as a human carcinogen. This metal has no physiological function in humans and is deemed a toxicant. Consequently, investigations into the biological activity of cadmium coordination compounds (Cd-CCs) have been scarce. However, cadmium toxicity is comparable to the toxicity of noble metals such as platinum and palladium,[1] whose complexes are studied to a great extent and some of them are approved for cancer treatment.[2] In addition, some studies indicate that cadmium toxicity depends on the form it exists in. Depending on the ligands utilized in their synthesis, cadmium complexes may exhibit good biological activity.[3]

The interest in the biological activity of cadmium complexes has been growing in recent years. Emerging data indicate that they directly target DNA and inhibit the incorporation of 3H-thymidine into DNA. Cadmium complexes also inhibit various protein targets such as proteasomal chymotrypsin-like, proteasomal deubiquitinase, histone deacetylase, telomerase and the respiration of tumor cells. They show potent anticancer activity and can kill cancer cells via programmed cell death apoptosis.[4]

Nowadays, there is an evident crisis in designing and developing a novel class of organic compounds as antibiotics. Namely, most of the compounds in clinical trials are derivatives of already-known antibiotics, whereas the number of new structural classes is limited. It is reasonable to expect that antibiotics, which are organic compounds, will be short-term solutions and that bacteria will develop resistance to these compounds in a short period. The solution to this is metal coordination compounds, which cover different chemical spaces when compared to purely organic compounds.[5] Consequently, the antimicrobial activity of Cd-CCs has been studied in recent years and promising results have been obtained.[6] Cd-CCs show better activities when compared to corresponding ligands, coordination compounds of other metals and standard antibiotics.[7–12]

Apart from the studies dealing with biological activity, Cd-CCs show interesting vapourchromic,[13] thermochromic,[14,15] photochromic[13,16–18] and photophysical[14,15,19–21] properties and are studied as chemosensors for cations and nitroaromatic explosives[17,22–24]. Some Cd-CCs exhibit promising photocatalytic,[25, 26] catalytic,[21,27–29] and CO_2 fixing properties.[30,31] Cd-CCs may serve as nanocrystals shell growth[32] and vapour deposition precursors,[33] as well as programmable triboelectric nanogenerators.[34] Finally, some Cd-CCs mimic organophosphate pesticide degrading enzymes[35] and show potent antioxidant properties.[36–39]

Thiazolyl hydrazones (THs) are compounds that show various activities, including antimicrobial and antioxidant activity.[40] In our previous work, we determined the potent anticancer, antibacterial and antioxidant activity of pyridine-based TH ligands and their Co (III) complexes.[40–43] We have also investigated the spectroelectrochemical properties of Co (III) complexes. As the goal of this study, we set the preparation of Cd(II) complexes with the following pyridine-based THs (*E*)-4-(4-methoxyphenyl)-2-(2-[pyridine-2-ylmethylene]hydrazinyl)thiazole (HLS^2) and (*E*)-2-(2-[pyridine-2-ylmethylene]hydrazinyl)-4-(p-tolyl)thiazole (HLS^3) ligands (Figure 1), as well as the investigation of their structural, thermal, spectroelectrochemical, antimicrobial and antioxidant properties. We have designed the complexes with thiazolyl and hydrazone groups to increase the electrochemical and optoelectrochemical functionality due to their possible redox activity and intense spectral changes under electron transfer processes in connection with their application for various display technologies, such as electrochromism.

2 | EXPERIMENTAL DETAILS

2.1 | Chemicals

All the employed reagents were of analytical grade and used without further purification. 2-Pyridinecarboxaldehyde (99%), 2-bromo-4′-methylacetophenone and 2-bromo-4′-methoxyacetophenone (98%) were obtained from Acros Organics, whereas thiosemicarbazide (99%) was obtained from Alfa Aesar, tetra butylammonium perchlorate (TBAP) and cadmium acetate dihydrate (98%) from Sigma Aldrich. All solvents (ethanol 96%, methanol, methylene chloride (DCM), dimethylsulfoxide (DMSO), dimethyl formamide (DMF), tetrahydrofurane (THF) and cyclopentane were of reagent purity and used without further purification.

2.2 | Physical measurements

Elemental analyses (C, H, N, S) were performed by the standard micro methods using the ELEMENTAR Vario EL III CHNS/O analyzer. Infrared spectra (IR) were recorded on a Thermo Scientific Nicolet SUMMIT FT-IR Spectrometer at the wavelength of 4,000–450 cm^{-1}, using the attenuated total reflection (ATR) technique. Abbreviations used in IR spectroscopy: w-weak; m-medium; ms-medium strong; s-strong; vs-very strong. The NMR spectra were recorded on a Bruker Avance 500 equipped with

a broad-band direct probe. One-dimensional (1-D) and 2D NMR spectra were recorded at 298 K in $CDCl_3$ with tetramethyl-silane (TMS) as an internal standard. Chemical shifts (δ) are given in ppm. Abbreviations used for NMR spectra: s-singlet, d-doublet, t-triplet and m-multiplet. Atom numbering is given in Figure 1. At ambient temperature (298 K), molar conductivity measurements were performed on a Crison multimetre MM41 instrument. Thermal data were collected using a TA Instruments SDT Q600 thermal analyzer coupled to a Hiden Analytical HPR20/QIC mass spectrometer. The decomposition was carried out from room temperature to 500 °C at a heating rate 10 °C min^{-1} in argon and air as carrier gases (flow rate = 50 cm^3 min^{-1}). The sample holder/reference is an alumina crucible/empty alumina crucible. The sample mass was 3–5 mg. Selected ions between m/z = 1–90 were monitored in multiple ion detection modes (MIDs).

2.3 | Synthesis of the ligands HLS^2 and HLS^3

The ligands HLS^2 and HLS^3 were synthesized according to the literature procedure.[43] The data obtained by elemental analysis and spectral characterization of the ligands are in agreement with the previously published results.[43]

2.4 | Synthesis of complexes $[Cd(LS^2)_2]$ (1) and $[Cd(LS^3)_2]$ (2)

1: Into suspension of HLS^2 (0.100 g; 0.32 mmol) in 10 ml MeOH, a solid $Cd(CH_3COO)_2 \cdot 2H_2O$ (0.086 g; 0.32 mmol) was added. The mixture was refluxed and stirred for 1 h. The resulting red precipitate was filtered off, washed several times with cold MeOH, followed by drying under vacuum. After recrystallization by vapour diffusion of cyclopentane into a solution of the crude precipitate in DCM, quality red single crystals were obtained. Yield of the recrystallized product: 0.045 g (19%). Anal. Calcd. for $C_{32}H_{26}CdN_8O_2S_2$ (%): C, 52.57; H, 3.58; N, 15.33; S, 8.77. Found: C, 52.19; H, 3.52; N, 15.09; S, 9.02. Λ_M ($1 \cdot 10^{-3}$ M, MeOH) = 7.24 $\Omega^{-1}cm^2mol^{-1}$. IR (ATR, ν_{max}/cm^{-1}): 3122 (w), 2,996 (w), 2,937 (w), 2,831 (w), 2,778 (w), 2,629 (w), 2,176 (w), 2056 (w), 2031 (w), 1,591 (ms), 1,538 (ms), 1,492 (m), 1,393 (vs), 1,329 (s), 1,238 (s), 1,209 (s), 1,174 (ms), 1,108 (ms), 1,085 (ms), 1,026 (ms), 888 (ms), 842 (m), 768 (m), 738 (m), 676 (m), 634 (m) and 610 (m). ^{1}H NMR (500.26 MHz, $CDCl_3$) δH: 3.73 (s, 1H, H–C16), 6.21 (s, 1H, H–C8), 6.65 (d, 2H, H–C12 = H–C14), 6.95 (m, 1H, H–C4), 7.04 (d, 1H, H–C2), 7.24 (m, 2H, H–C11 = H–C15), 7.53 (t, 1H, H–C3), 7.89 (m, 1H, H–C6) and 7.98 (d, 1H, H–C5). ^{13}C NMR (126.0 MHz, $CDCl_3$) δC: 55.34 (C16), 99.06 (C8), 113.61 (C12 = C14), 122.59 (C4), 122.96 (C2), 127.25 (C11), 127.32 (C15), 129.72 (C6), 138.40 (C3), 148.20 (C5), 149.43 (C10), 150.84 (C1), 155.43 (C7), 159.28 (C13) and 182.20 (C9).

2: Into suspension of HLS^3 (0.100 g; 0.34 mmol) in 10 ml MeOH, a solid $Cd(CH_3COO)_2 \cdot 2H_2O$ (0.090 g; 0.34 mmol) was added. The mixture was refluxed and stirred for 1 h. The resulting red precipitate was filtered off, washed several times with cold MeOH, followed by drying under vacuum. After recrystallization by vapour diffusion of cyclopentane into a solution of the crude precipitate in DCM, quality red single crystals were obtained. Yield of the recrystallized product: 0.053 g (22%). Anal. Calcd. for $C_{32}H_{26}CdN_8S_2$ (%): C, 54.97; H, 3.75; N, 16.03; S, 9.17. Found: C, 54.24; H,3.82; N,16.06; S, 9.21. Λ_M ($1 \cdot 10^{-3}$ M, MeOH) = 4.19 $\Omega^{-1}cm^2mol^{-1}$. IR (ATR, ν_{max}/cm^{-1}): 3109 (w), 3,012 (w), 2,913 (w), 2,863 (w), 2,775 (w), 2,651 (w), 1,590 (ms), 1,535 (ms), 1,493 (w), 1,474 (w), 1,393 (vs), 1,321 (s), 1,297 (ms), 1,236 (m), 1,207 (s), 1,183 (ms), 1,151 (ms), 1,109 (s), 1,085 (s), 1,003 (m), 885 (m), 839 (m), 814 (m), 769 (w), 744 (w), 723 (w), 675 (w), 638 (w), 608 (w) and 532 (w). ^{1}H NMR (500.26 MHz, $CDCl_3$) δH:

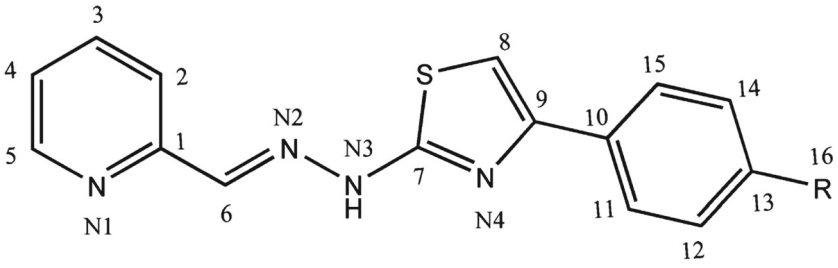

Ligands		Complexes	
Label	R	Label	Bruto formula
HLS^2	OMe	**1**	$[Cd(LS^2)_2]$
HLS^3	Me	**2**	$[Cd(LS^3)_2]$

FIGURE 1 Labelling of the ligands and complexes used in this study.

2.22 (s, 1H, H–C16), 6.28 (s, 1H, H–C8), 6.94 (m, 3H, H–C3 = H–C12 = H–C14), 7.05 (d, 1H, H–C2), 7.22 (d, 2H, H–C11 = H–C15), 7.53 (t, 1H, H–C4) and 7.93 (m, 2H, H–C5 = H–C6). ^{13}C NMR (126.0 MHz, $CDCl_3$) δC: 21.11 (C16), 99.98 (C8), 122.69 (C3), 123.06 (C2), 125.86 (C11 = C15), 128.92 (C12 = C14), 129.92 (C6), 131.57 (C7), 137.70 (C13), 138.43 (C4), 148.21 (C5), 149.67 (C10), 150.74 (C1) and 181.88 (C9).

The IR, ^{1}H and ^{13}C NMR spectra of the complexes are shown in electronic supplementary information (ESI, Figures S1–S14).

2.5 | X-ray crystallography

At room temperature, single-crystal data were collected using an Xcalibur Ruby Nova diffractometer with copper radiation ($\lambda = 1.54183$ Å). Data reduction and cell refinement were carried out using the CRYSALIS PRO software,[44] and standard multiscan absorption correction was applied. Structures were solved by direct methods with SIR2014[45] and refined by a full-matrix least-squares refinement based on F^2, with SHELXL.[46] Molecular illustrations were prepared with Mercury,[47] which is included in the WinGX package.[48] Calculations of molecular geometries and crystal packing parameters were performed with Platon.[49] Hydrogen atoms were included in their geometrically calculated positions and refined according to the riding model. Crystal data, data collection and refinement parameters are summarized in Table S1 (ESI). CCDC 2177360–2,177,361 contain the supplementary crystallographic data. These data can be obtained free of charge via http://www.ccdc.cam.ac.uk/conts/retrieving.html, or from the Cambridge Crystallographic Data Centre, 12 Union Road, Cambridge CB2 1EZ, UK; e-mail: deposit@ccdc.cam.ac.uk.

Powder X-ray diffraction (PXRD) experiments were conducted on a Rigaku SmartLab X-ray diffractometer in θ-θ geometry (the samples in a horizontal position) in parafocusing Bragg–Brentano geometry using D/teX Ultra 250 strip detector in 1D standard mode with CuK$\alpha_{1,2}$ radiation source ($U = 40$ kV and $I = 30$ mA). The PXRD patterns were collected in 5–65° 2θ range, with a step of 0.01° min^{-1}.

2.6 | Hirshfeld surface analysis

For Hirshfeld surface analysis,[50] the CIF files, with normalized values of the bond lengths with hydrogen atoms, were used as input files. The Hirshfeld surfaces and 2D fingerprint plots were generated using CrystalExplorer[51,52]. The distance from the Hirshfeld surface to the nearest nucleus outside the surface is marked as d_e, whereas d_i is the corresponding distance to the nearest nucleus inside the surface. The d_{norm} values are mapped onto the Hirshfeld surface using a red–blue–white colour scheme; the red colour corresponds to closer contacts with a negative d_{norm} value, the blue colour corresponds to longer contacts with a positive d_{norm} value and the white colour is for contacts where the d_{norm} value is zero. 2D fingerprint plots were represented with a combination of d_e and d_i distance values in the range 0.4–2.8 Å.

2.7 | Computational methods

Quantum-chemical calculations were performed to estimate the strength of interactions between Cd(II) complexes observed in the investigated crystal structures in order to describe the crystal packing within analyzed structures. Calculations were performed in the Gaussian09 program,[53] using the Austin-Frisch-Petersson (APFD) functional, *6-31 g*** basis set for nonmetals and *lanl2dz* basis set for Cd.

For docking studies, the structures of **1** and **2** were optimized by APFD method, with 6–31 g** basis set for nonmetal atoms and *lanl2dz* basis set for Cd. The Merz–Kollman atomic charges were calculated for all atoms at the same level, according to the scheme via the RESP procedure. The structure of DNA was extracted from Protein Data Bank (pdb code: 1BNA).[54] The chosen structure represents double-stranded DNA with two G ≡ C rich region and one A = T rich region, between them.

The AutoDockTools software was used to prepare the DNA structure and generate grid and docking parameter files, whereas the AutoDock 4.2 programme was used for molecular docking calculations.[55] A grid box containing the whole structure of selected DNA was made to accommodate investigated Cd complexes. The Lamarckian genetic algorithm was used as the search method for virtual screening, with 100 runs for each docking screen. The Discovery Studio software was used to visualize and analyze the results of the docking study.[56]

2.8 | Determination of stability constants

The stability constant values for the complexes formed as a result of the interaction of HLS^2 and HLS^3 ligands with Cd^{2+} ions were determined using the spectrophotometric titration method. The UV–Vis Thermo Scientific Evolution 300 spectrophotometer was used to record electronic spectra in the range of 200–600 nm with a spectral bandwidth of 1 nm. Solutions of the ligands were prepared in

methanol directly before the measurements, and their concentrations were $c = 4.24 \cdot 10^{-5}$ M and $c = 3.39 \cdot 10^{-5}$ M for HLS^2 and HLS^3, respectively. The ligands' concentrations remained unchanged throughout the titration process. The ligands were titrated with cadmium acetate (recrystallized and dried at 170 °C) dissolved in the solution of the analyzed ligand. A magnetic stirrer was placed in the measuring cuvette to continuously mix the titrant with the analyte. A microtitration automatic Cerko-Lab system, equipped with a 1 ml Hamilton syringe, was used for titrant dosing. A single titration step was 8.31 µl. Measurements were carried out at 298 K. The titrations were repeated twice to ensure the repeatability of the results. The measurement data were processed in the OriginLab program.

The gradual and cumulative stability constants of the complexes were determined using the EQUID computational program.[57,58] It is based on an algorithm in which the equilibrium model of the solution is described based on the measurement data.[59,60] The details regarding the stability constant calculations are given in ESI.

2.9 | Electrochemistry and *in situ* spectroelectrochemistry

The cyclic voltammetry (CV), square wave voltammetry (SWV) and spectroelectrochemical measurements were carried out with a Gamry Reference 600 potentiostat/galvanostat utilizing a three-electrode configuration at 25 °C by following the procedure conducted in our previous papers.[61,62] Glassy carbon electrode (GCE), Pt wire and Ag/AgCl electrode served as the working, counter and reference electrodes, respectively. TBAP dissolved in DMSO was employed as the supporting electrolyte at a concentration of 0.10 M. UV–Vis absorption spectra were measured using Ocean Optics QE65000 diode array spectrophotometer. *In situ* spectroelectrochemical measurements were carried out by utilizing a Pt tulle working electrode in the three-electrode configuration of a thin-layer quartz spectroelectrochemical cell at 298 K.

2.10 | Antioxidant capacity evaluation

The total antioxidant capacity (TAC) of synthesized compounds was compared in two electron-transfer (ET)-based spectrophotometric tests,[63–65] using a Shimadzu UV-2550 spectrophotometer. The first use the 2,2′-azinobis(3-ethylbenzothiazoline-6-sulfonic acid) (ABTS) radical decolourization method. The reduction of the stable blue–green ABTS cation radical by an antioxidant is measured by suppressing its characteristic long-wave absorption spectrum. An ABTS radical was generated during a chemical reaction between equal volumes of aqueous solutions of 7 mM ABTS diammonium salt and 2.45 mM potassium persulfate.[63] This mixture was kept at room temperature in darkness throughout the night. Before analysis, the blue–green colour of the radical solution was diluted with phosphate buffer saline (PBS, pH = 7.4) to obtain a final absorbance value of 0.900 ± 0.020, measured at 734 nm. Aliquots of 100 µl of the properly diluted complexes in DMSO or Trolox solutions (with concentrations ranging from 0 to 1 mM) were added to 1 ml of ABTS solution, and the absorbance value was measured 15 min after mixing. The second test was a Ce (IV)-based reducing capacity (CERAC) method, a simple, sensitive and low-cost assay, where the determination of the remaining Ce (IV) species at 320 nm was performed after oxidation of all antioxidants in the solution with cerium (IV) sulfate in dilute sulfuric acid at room temperature.[64] The reaction mixture contained 1,050 µl of 1 M Na_2SO_4, 150 µl of MilliQ water, 150 µl of the sample (in the same concentrations as in the ABTS assay) and 150 µl of 2 mM Ce $(SO_4)_2$ in 0.3 M H_2SO_4. After the mixture stood for 30 min at room temperature, the absorbance was measured and then corrected for the background sample absorbance.[65] The scavenging (ABTS) or reducing (CERAC) capability was calculated using the following equation:

$$\text{The percentage inhibition}(\%) = \left[\left(A_{\text{Control}} - A_{\text{Sample}}/A_{\text{Control}}\right) \times 100\right],$$

where A_{Control} is the initial concentration of the chromophore and A_{Sample} is the absorbance of the remaining concentration of chromophore in the presence of an antioxidant (analyzed samples). For comparison purposes, IC_{50} values were calculated for each compound. IC_{50} value is the concentration of the sample required for a 50% inhibition activity.

2.11 | Antimicrobial activity evaluation

Antimicrobial activity was tested against a panel of the following microorganisms: Gram-negative bacteria *Escherichia coli* (ATCC 25922), *Pseudomonas aeruginosa* (ATCC 9027), *Proteus hauseri* (ATCC 13315), *Klebsiella pneumoniae* (ATCC 10031), *Salmonella enterica* subsp. *enterica* serovar Enteritidis (ATCC 13076); Gram-positive bacteria *Staphylococcus aureus* (ATCC 6538), *Clostridium sporogenes* (ATCC 19404), *Micrococcus luteus* (ATCC 4698), *M. luteus* (ATCC 10240); yeasts *Candida albicans* (ATCC 10231) and *Saccharomyces cerevisiae* (ATCC

9763); fungal strain *Aspergillus brasilliensis* (ATCC 16404).

Antimicrobial activity was evaluated using the broth microdilution method according to the protocol of the National Committee for Clinical Laboratory Standards.[66] The 96-well plates were prepared by dispensing 100 µl of Mueller–Hinton broth for bacteria and Sabouraud dextrose broth for yeasts and fungi into each well. An aliquot of 100 µl from the stock solution of the tested compounds (concentration 10 mg·mL^{-1} in DMSO) was added to the first row of the plate and double diluted. A suspension of bacteria and yeasts was prepared in sterile 0.9% saline. Suspension turbidity evaluation was conducted by comparison with 0.5 McFarland's standard. A 10 µl of diluted bacterial, yeast or spores suspension was added to each well to give a final concentration of $5{\cdot}10^5$ CFU·mL^{-1} for bacteria and $5{\cdot}10^3$ CFU·mL^{-1} for yeast and fungi (CFU is colony forming unit). Erythromycin served as positive control for bacteria, whereas amphotericin B served as a positive control for yeasts and fungi. The inoculated plates were incubated at 37 °C for 24 h for bacteria and at 28 °C for 48 h for yeasts and fungi. The bacterial growth was visualized by adding 20 µl of 0.5% 2,3,5-triphenyltetrazolium chloride (TTC) aqueous solution.[67] A minimum inhibitory concentration (MIC) was defined as the lowest concentration of the compounds that inhibited bacterial and fungi growth (red-coloured pellet at the bottom of the wells after the addition of TTC).

3 | RESULTS AND DISCUSSION

3.1 | Chemistry

In order to prepare Cd complexes with the anionic form of HLS^2 and HLS^3 ligands, into methanol suspension of the appropriate ligand, the solid $Cd(CH_3COO)_2{\cdot}2H_2O$ was added in the molar ratio of 2: 1 (ligand: metal). The obtained mixtures were heated under reflux for 1 h and the red precipitates were filtered off. Red single crystals of **1** and **2**, suitable for X-ray diffraction analysis, were obtained after a few days by vapour diffusion of cyclopentane into the solution of the crude precipitates in DCM. Results of elemental analysis indicate that two ligands are coordinated to the cadmium centre in anionic form. These results are in agreement with the general formulas of the complexes given in Figure 1. Values of molar conductivity are also in agreement with the proposed general formulas. Because of their nonelectrolyte nature, **1** and **2** are not soluble in polar solvents like water, methanol, ethanol and acetonitrile. They are soluble in THF, DCM, DMF and DMSO.

The IR, ^{1}H and ^{13}C NMR spectra of the complexes are shown in ESI (Figures S1–S14). The absence of symmetric and asymmetric stretching modes of OH bonds in the IR spectra of the complexes (in the range of 3,500–3,200 cm^{-1}) points to the absence of crystalline water or methanol molecules in the structures. The highest value of the chemical shift in the ^{1}H NMR spectra of the ligands belongs to the hydrogen atom H–N3.[43] This signal is absent in the ^{1}H NMR spectra of both complexes, thus the corresponding ligands are coordinated to Cd(II) in their monoanionic form.

3.2 | Molecular and crystal structures

A summary of the crystallographic data of the complexes is given in Table S1 (ESI). ORTEP drawings of **1** and **2** are depicted in Figure 2. **1** crystallizes in the triclinic *P*-1, while **2** crystallizes in the monoclinic $P2_1/c$ space group. In both complexes, two meridionally placed ligands are coordinated to the central Cd(II) ion. The ligands are coordinated in monoanionic form via pyridine, imine and thiazole nitrogen atoms, forming two five-membered chelate rings around the central metal ion. The six donor nitrogen atoms form a slightly distorted octahedron. The coordination sphere geometry parameters are given in Table S2 (ESI).

The packing of the molecules in the crystal structures of **1** and **2** is depicted in Figure S15 (ESI), whereas the results of energy calculations for both complexes are given in Tables S3 and S4 (ESI), along with a detailed discussion of the interactions responsible for the crystal packing formation of both complexes. In short, in the crystal structure of **1**, the centrosymmetric dimer is formed by C–H···N, C–H···O and C–H···S noncovalent interactions. The dimers interact with each other, forming 1-D chains via C–H···N, C–H···O, and C–H···S interactions, which are further connected into 2-D layers via C–H···N, C–H···S, C–H···π and pyridine-pyridine aromatic interactions. The 3-D supramolecular structure is based on the packing of 2-D layers along the *b*-crystallographic axis. Each 2-D layer interacts with the adjacent layer by C–H···π and PILO (parallel interaction at large offsets),[68] C–H···S and C–H···O interactions. In the crystal structure of **2**, 1-D chains are formed parallel to the *b*-crystallographic axis via non-classical PILO and C–H···π interactions. The orientation of complex **2** in 1-D chains makes the benzene rings available for interactions with the environment with a formation of 2-D layers via C–H···π and stacking interactions. These 2-D layers are further connected via C–H···N, C–H···S, C–H···π, PILO and hydrophobic interaction, forming a 3-D crystal packing of **2**.

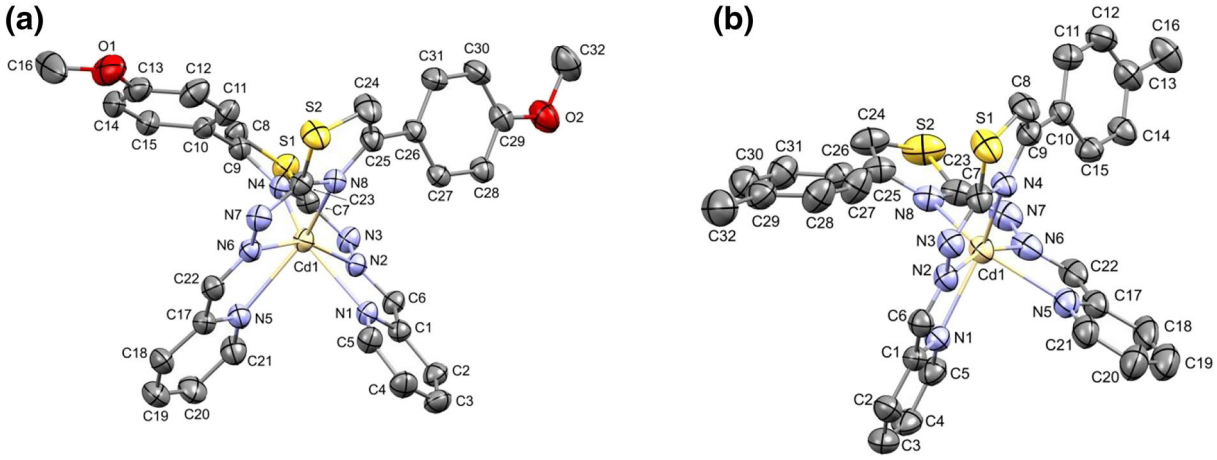

FIGURE 2 ORTEP drawings of molecular structures of **1** (a) and **2** (b). Thermal ellipsoids are shown at the 30% probability level. Hydrogen atoms are omitted for clarity.

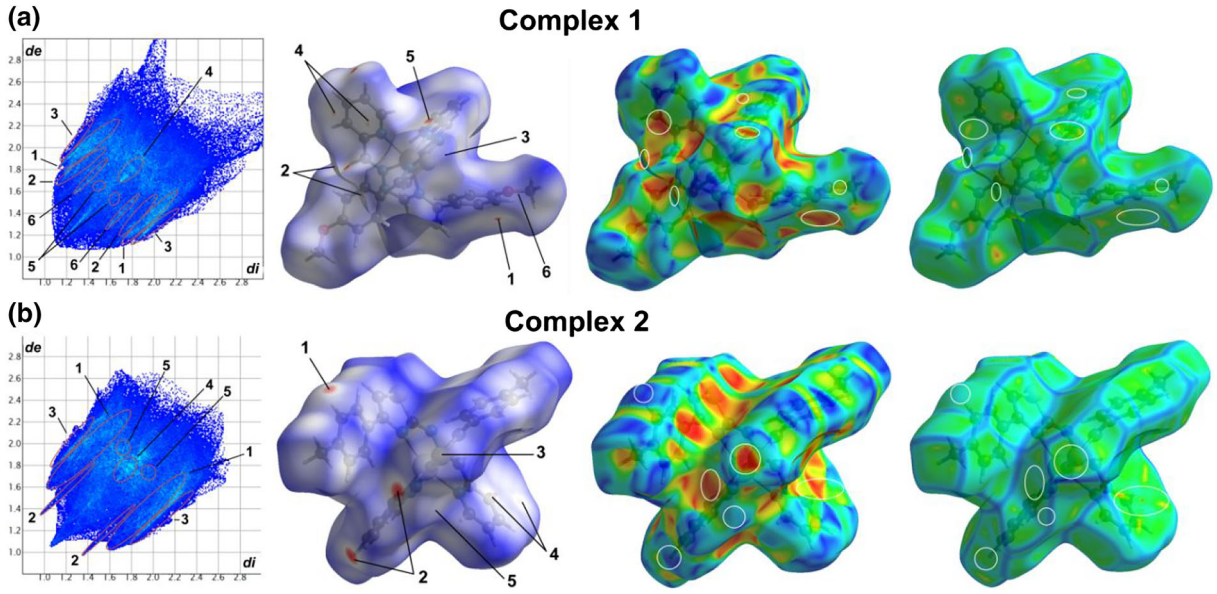

FIGURE 3 2-D fingerprint plot, Hirshfeld surface mapped with d_{norm}, shape index, and curvedness for **1** (A) and **2** (B).

PXRD analysis was performed on both single-crystal samples, which confirmed that the bulk samples are single-phase systems (Figure S16, ESI). Since other phases are absent, it can be concluded that the obtained single crystals of **1** and **2** are stable in the air under standard conditions and during pulverization.

3.3 | Hirshfeld surface and fingerprint plot analysis

The Hirshfeld surface and corresponding 2-D pseudosymmetric fingerprint plots were calculated to quantify the intermolecular interactions present in the crystal structures of **1** and **2**. Significant classical and nonclassical intermolecular interactions are depicted in Figure 3. On 2D pseudosymmetric fingerprint plots, the relative contributions of each interaction are marked with red circles. Also, the interactions can be observed in the shape-index plot as red and blue regions, as well as in the curvature plot as a flat zone in the same position on the surface as in the shape-index plot. White circles mark the regions of the surfaces through which the complexes interact. The relative contribution of different types of interactions in both complexes is very similar (Table 1). In the crystal structure of **2** there are five main types of interactions. In the case of **1** there is one additional O···H interaction as a consequence of the presence of a methoxy group in the structure. The dominant interactions in both complexes are C···H, followed by S···H and N···H interactions. In the case of **2**, O···H interactions also have a significant contribution. The S···N interactions have a relatively small contribution to the crystal packing, but they are stronger in the crystal packing of **1** and appear as red spots on the

Interaction number	Interaction type	1	2
		Relative contribution (%)	
1	C···H	26.2	27.5
2	N···H	9.7	9.0
3	S···H	11.1	12.2
4	C···C	2.5	3.7
5	S···N	0.9	0.7
6	O···H	6.0	/

TABLE 1 Relative contribution (in %) of different interaction types in **1** and **2**

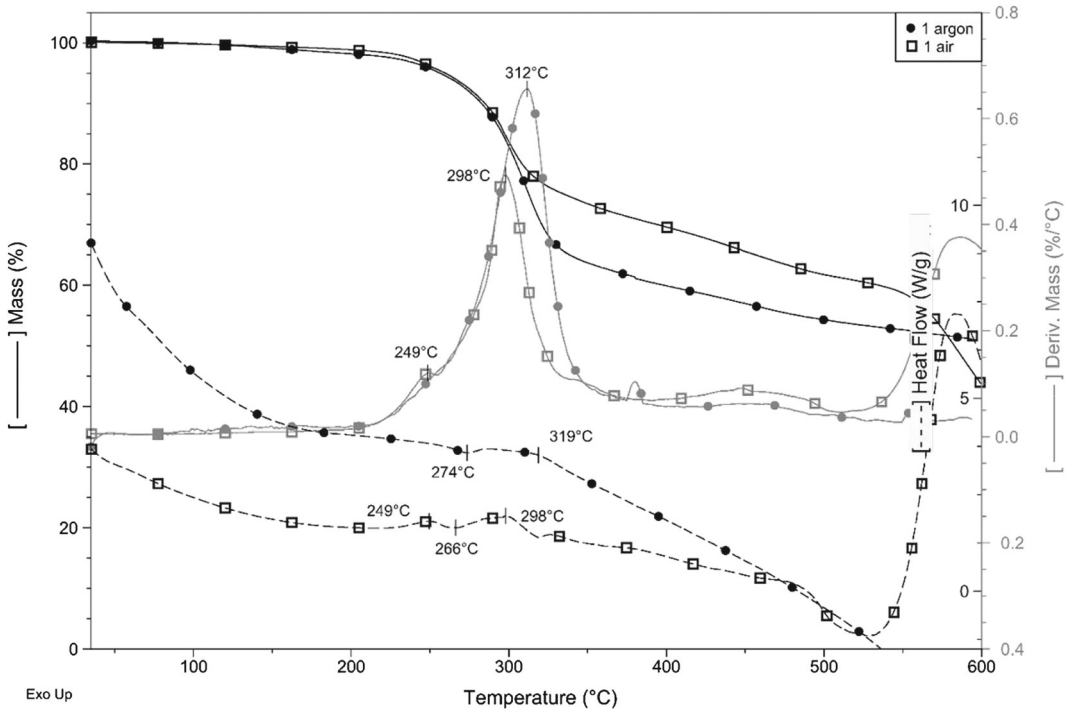

FIGURE 4 TG, DTG and DSC curves of **1** in argon and air.

Hirshfeld surface (Figure 3). Also, there were no interactions involving the central metal ion.

Despite the fact that C···H interactions are the most dominant, they are significantly weaker compared to hydrogen bonds, which include S, N and O atoms. Consequently, both crystal structures are governed by S···H, and N···H hydrogen bonds. Additionally, O···H hydrogen bonds have a significant contribution to the crystal packing of **1**.

3.4 | Thermal properties of 1 and 2

To study the possible application of new compounds, it is crucial to determine their thermal stability and general thermal properties. **1** and **2** are examined by simultaneous thermogravimetric-differential scanning calorimetric analysis in an inert and oxidative atmosphere. In argon, a slight mass decrease (about 2%) was observed on the thermogravimetric (TG) curve of both compounds; **1** and **2** begin to lose mass at room temperature. Since the compounds were completely dry, this small mass loss is most probably the result of the fragmentation of the complex compounds. The decomposition process becomes more intensive at 218 and 222 °C, the onset temperatures for **1** and **2**, respectively. The decomposition processes of **1** (Figure 4) are completely overlapped, with only one derivative TG (DTG) maximum at 312 °C. The mass loss in this step is 38.2%, which is somewhat less than the loss of one TH ligand (42.31%). Above 350 °C, the decomposition of **1** slows and does not complete up to 600 °C.

Differently, on the TG and DTG curves of **2** two decomposition steps can be distinguished up to 400 °C

with DTG maxima at 265 and 349 °C (Figure S17, ESI). The corresponding mass losses are 19.6 and 27.1%, respectively. Their sum (46.7%) is slightly higher than the mass percentage of one ligand molecule (41.96%). Above 400 °C the decomposition of **2** slows and does not complete until 600 °C.

The decomposition mechanism of **1** in the air is somewhat different compared to the decomposition mechanism observed in argon (Figure 4). Up to 200 °C, the two decomposition processes are almost the same, but above this temperature, a small mass loss of 4.0% is detected with a DTG peak at 254 °C. The next decomposition step, with mass loss of 28.1%, is less than that in argon (39.1%), with the DTG peak at 302 °C. Up to 480 °C, there are no other differences between decomposition processes in inert and oxidative atmospheres. Above this temperature, the oxidative decomposition of TH type ligand begins. The final residue is most probably CdO. The formation of other IR-active products is excluded by IR spectra. Its mass percentage (15.9%) is somewhat less than calculated (17.56%).

The decomposition processes of **2** in the air above 230 °C are also different compared to thermal data recorded in argon. These processes overlap more in oxidative atmospheres than in inert atmospheres, with DTG peak maxima at 256, 318, 481 and 596 °C (Figure S17, ESI). The total mass loss up to 500 °C is less in the air (23.5 and 12.6%) than in argon (19.3 and 26.2%). Above 500 °C the organic ligand burns out. The final residue is 24.9%, which is significantly more than the calculated value (18.37%).

The thermal decomposition of **1** in argon up to 290 °C is endothermic with a small peak at 274 °C, above this temperature, the decomposition becomes slightly exothermic with a peak maximum at 318 °C. In air, the heat effects of the decomposition of **1** are different. The first exothermic DSC peak appears at 249 °C, followed by an endothermic peak with a maximum at 266 °C. After that, a prolonged exothermic but small- intensity process is observed on the curve with a peak maximum at 298 °C, which also changes into an endothermic process and gives a peak at 319 °C. Exothermic combustion of TH ligand occurs above 450 °C.

The heat flow curves of **2** in argon and air are the same up to 300 °C, with endothermic peaks at 219 and 218 °C. The next peak in argon appears at 342 °C and it is endothermic. In contrast, there is a slight, then an intensive exothermic peak in air at 325 and 481 °C. Exothermic oxidative degradation processes occur above 500 °C.

Besides TG and DSC analysis, **1** and **2** were analyzed by online coupled TG-MS measurements also. Even though both compounds lose about 2% of their mass up to about 200 °C, this mass loss occurs over a wide temperature range and does not give any significant peak in the mass spectra. The main decomposition processes above 200 °C are followed by evolution of fragments, characteristic for the THs ligand of $m/z = 15$ (CH_3^+), 27 (CHN^+), 28 (CH_2N^+, N_2^+), 31 (CH_3O^+ in 153), 36 (C_3^+), 38 (C_2N^+) and 44 ($CH_4N_2^+$). The low-intensity peak of fragment 32 m/z most probably belongs to S^+.

3.5 | Determination of stability constant values

Based on the analysis of the spectrophotometric titration curves, the number of equilibria, the stoichiometry and the stability of complexes formed with the Cd^{2+} ion (whose source was cadmium acetate) were determined (Figure 5). The spectral effects observed during the titration of HLS^2 and HLS^3 with $Cd(CH_3COO)_2$ are similar to the changes in the UV–Vis spectra obtained by titration of these compounds with cadmium perchlorate and cadmium nitrate.[2]

The positions of the ligands' absorption maxima and the resulting complexes are summarized in Table 2. When comparing the type of a substituent (methoxy or methyl group) within the ligands, slight differences were observed, both in the original position of the ligand bands and in the spectral effects associated with complexation. However, in both cases, an increase in the intensity of the ligand band at about 200 nm and a reduction of the intensity of the ligand absorption maxima at ca. 270 and 355 nm were observed. In the case of the maximum at ca 270 nm, its shift toward shorter wavelengths (blue shift) is also observed for both ligands. Moreover, a new, intense absorption maximum in the visible region of the spectrum (ca. 450 nm) has formed (Figure 5a and b). A solution colour change from light yellow to orange was observed during the complexation.

The acetate anion induces a solvent protolysis reaction, thus making the pH of the solution alkaline. Consequently, the ligands undergo deprotonation and coordinate to Cd^{2+} in the anionic form via a pyridine, imine and thiazole nitrogen atom. The performed titrations allowed us to determine the dependence of the changes in absorbance on the molar metal: ligand ratio (Figure 5c and d). This enabled the assessment of the obtained complex ion stoichiometry and the calculation of stability constant values. For both ligands, the curve inflection is observed on the absorbance vs c_M/c_L graphs, which indicates the formation of $[ML_2]$ type complexes. The determined values of the cumulative stability constants (β_{12}) are 9.88 and 9.71 for **1** and **2**, respectively, which indicates significant stability of these forms of

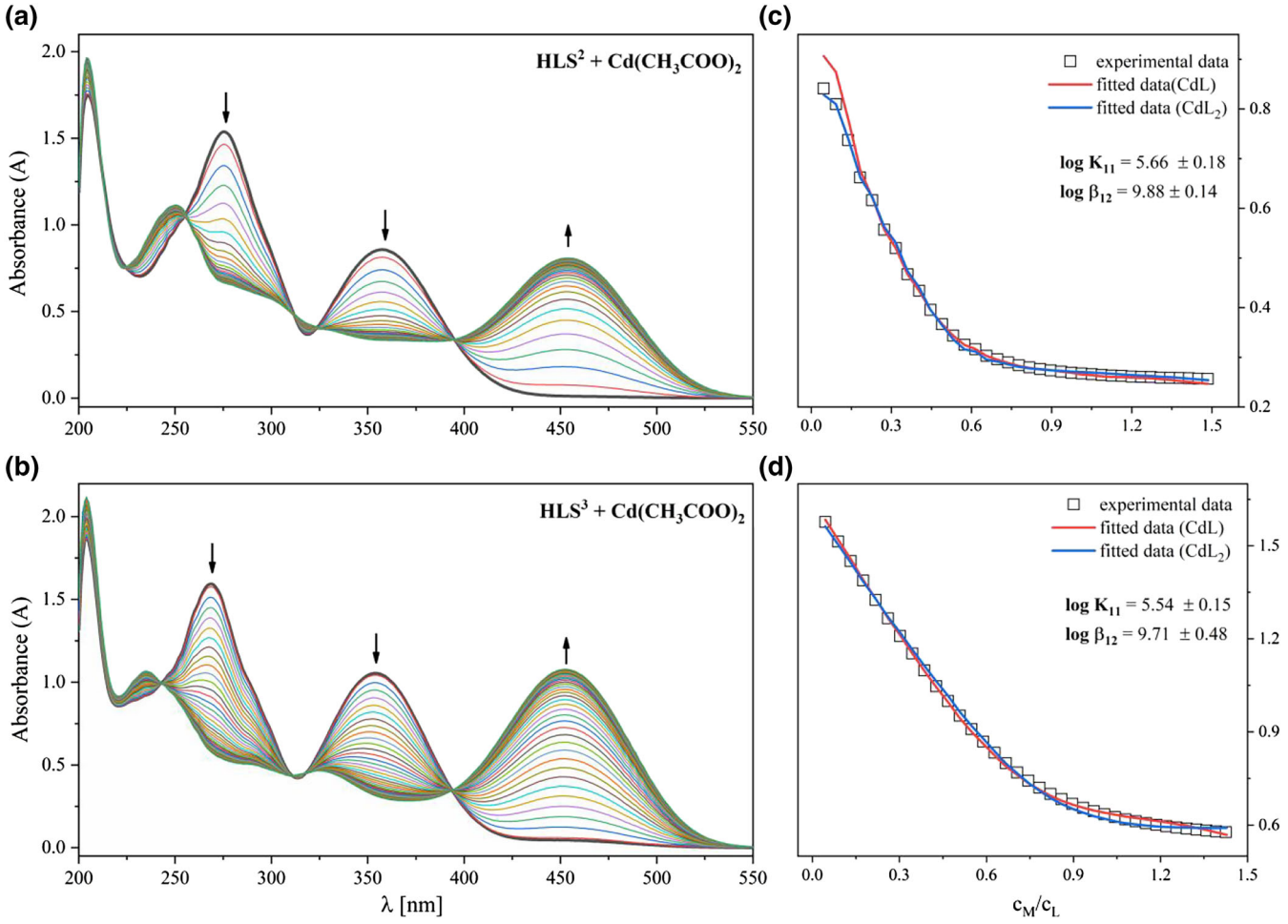

FIGURE 5 UV–Vis spectra demonstrating changes during titration of HLS^2 (a) ($c_L = 4.24 \cdot 10^{-5}$ M) with $Cd(CH_3COO)_2$ solution ($c_M = 4.50 \cdot 10^{-4}$ M) and HLS^3 (b) ($c_L = 3.39 \cdot 10^{-5}$ M) with $Cd(CH_3COO)_2$ solution ($c_M = 3.61 \cdot 10^{-4}$ M) in methanol. The arrows indicate the direction of change with the addition of Cd^{2+} ions. The black bold line represents the starting point of the titration (ligand spectrum). Dependence graphs of HLS^2 (c) and HLS^3 (d) absorbance changes during titration versus molar metal–ligand ratio (c_M/c_L)- scatter, along with the data fitted from the calculations – red and blue lines.

Ligand	**λ_{max1} [nm]**	**λ_{max2} [nm]**	**λ_{max3} [nm]**		
HLS^2	205	275	357		
HLS^3	204	269	354		
Complex formed	**λ_{max1} [nm]**	**λ_{max2} [nm]**	**log K_{11}**	**log K_{12}**	**log β_{12}**
$[Cd(LS^2)_2]$ (**1**)	204	454	5.66 ± 0.18	4.22*	9.88 ± 0.14
$[Cd(LS^3)_2]$ (**2**)	204	453	5.54 ± 0.14	4.16*	9.71 ± 0.48

*$\log K_{12} = \log \beta_{12} - \log K_{11}$.

TABLE 2 Values of wavelengths maxima (λ_{max}) for the ligands and complexes. Values of gradual (K_{11}, K_{12}) and cumulative (β_{12}) stability constants (along with values of standard deviations) of the complexes formed with cadmium ions, using $Cd(CH_3COO)_2$ as a titrant

coordination in the solution. The values of β_{12} do not differ significantly from those obtained in the case of titration with salts of strong acids, in which the ligands were in the neutral (not deprotonated) form. However, it should be noted that the β_{12} constant includes gradual complexation reactions described by the equations eqS1 and eqS2 and expressed by the constants K_{11} and K_{12} (ESI).

When comparing the values of the latter for the titration of deprotonated (L^-) and nondeprotonated (HL) ligands, we notice a significant difference. For the complexes formed by the ligand containing methoxy group (HLS^2), these values were: log $K_{11} = 6.09$ and log $K_{12} = 3.86$ for the complexation of the ligand in the HL form.[2] However, in the case of the complexation process by the deprotonated ligand $(LS^2)^-$ they are: log

$K_{11} = 5.66$ and $\log K_{12} = 4.22$. This indicates an increase in the stability of the chelate complex with a stoichiometry M: L = 1: 2 relative to the 1: 1 form, and thus an increase in the complexation tendency in the coordination form $[Cd(LS^2)_2]$. The difference is even greater in the case of complexes formed by the ligand with a methyl substituent (HLS^3). The constants describing the stepwise attachment of nondeprotonated ligand (HL) were: $\log K_{11} = 6.11$ and $\log K_{12} = 3.06$. Nonetheless, in the experiment in which the cadmium ions are complexed by the deprotonated ligand form $(LS^3)^-$, the values of the constants are $\log K_{11} = 5.54$ and $\log K_{12} = 4.16$.

Summing up, comparing the values of constants describing the gradual attachment of deprotonated ligands to Cd^{2+} cation, relative to nondeprotonated ones, a decrease in the value of the constant associated with the one of the first ligand binding (K_{11}; ML 1:1 stoichiometry), and an increase in the value of the constant describing the attachment of the second ligand (K_{12}; ML_2 stoichiometry 1:2) was observed. These results prove the increase in stability of the chelate complex with deprotonated ligands in the solution.

3.6 | Electrochemical studies

It is well reported in the literature that (1,3-thiazol-2-yl) hydrazone derivatives can undergo successive $2e^-$ imine group (C=N) double bond reduction and $1e^-$ thiazole-based oxidation processes, which can be altered by the number of ligands present in the complexes, the type of the metal cation to which they are coordinated, and the type of the electrolyte in which the electrochemical analyses are performed.[69–71] The reduction of the hydrazone imine group results in hydrazo products, whereas further $2e^-$ reduction results in amine products.[69] Although $2e^-$ transfer reaction generally occurs in one step with the addition of $2H^+$ in aqueous solutions, these electrons can be transferred one by one in aprotic or non-acidic solutions.[72] THs are generally subjected to a $1e^-$ irreversible oxidation process, whose potential depends on the substituent environment of the ligands and electrolyte and electrode configurations[73,74]. For instance, Özkütük M. et al. reported the irreversible oxidation wave of six different thiazole-type ligands at around 1.0 V vs Ag/AgCl in DMSO/TBATFB electrolyte.[73] In another study, Kumar et al. reported the electrochemical responses of various thiazolyl-containing ligands between 0.80–1.25 V vs Ag/AgCl in $CHCl_3/Bu_4NPF_6$ electrolyte.[75] Studies also indicate that the redox features of these ligands can be tailored by the coordination of the ligands to various metal cations.[76–79] In the present study, we have examined the influence of the coordination of pyridil-based THs to Cd^{2+} cation, as well as the influence of the electrolyte to the redox responses of **1** and **2**. Voltammetric and *in situ* UV–Vis spectroelectrochemical characterizations of **1** and **2** in DCM/TBAP and DMSO/TBAP electrolytes on GCE were performed. Peak potentials of **1** and **2** in two different electrolytes derived from the CVs and SWVs are tabulated in Table 3. Both complexes showed one irreversible reduction and one irreversible oxidation wave within the potential window of DCM/TBAP electrolyte (Figure 6 and Figure S18, ESI). Due to the high electron releasing ability of the substituent environment in **2,** redox processes for **2** are slightly shifted towards the negative potentials compared to **1**. Controlled potential electrolysis (CPE) of the complexes at the redox potentials indicates $2e^-$ transfer nature of the reduction and oxidation waves of both complexes. The reduction and oxidation mechanisms of the complexes are represented in Scheme 1. The reduction waves can be easily attributed to the reduction of two imine groups of the complexes at the same potential with $2e^-$ transfer reaction. Similarly, two thiazole groups give two electrons at the same potential. While the $R(1)$ processes of the complexes are electrochemically quasireversible, with ΔE_p values around 80 mV at 25 mVs^{-1} scan rates (Figure 6a and Figure S19a, ESI), they become irreversible by increasing scan rates. These processes have chemically irreversible characteristics due to the

TABLE 3 Voltammetric data of the complexes

		Peak Potentials (V vs. Ag/AgCl at 100 mVs^{-1} scan rate)[a]				
Complexes	**Electrolyte**	***R*(1–1)[b]**	***R*(1–2)**	***R*(2)**	***O*(1–1)[c]**	***O*(1–2)**
1	DCM/TBAP	−1.61	-	-	0.80	-
2	DCM/TBAP	−1.65	-	-	0.61	-
1	DMSO/TBAP	−1.58	−1.81	−2.25	0.57	0.79
2	DMSO/TBAP	−1.55	−1.78	−2.19	0.60	0.72

[a]$E_{p,c}$ for reduction and $E_{p,c}$ for oxidation processes derived from SWVs.
[b]These values are for $R(1)$ processes in DC/TBAP electrolyte.
[c]These values are for $O(1)$ processes in DC/TBAP electrolyte.

possible succeeding chemical reactions with respect to the I_{pa}/I_{pc} ratios (around 0.25 at 100 mVs^{-1} scan rate as shown in Figure 6c and Figure S19c) and the I_{pc} vs. $\nu^{1/2}$ responses.

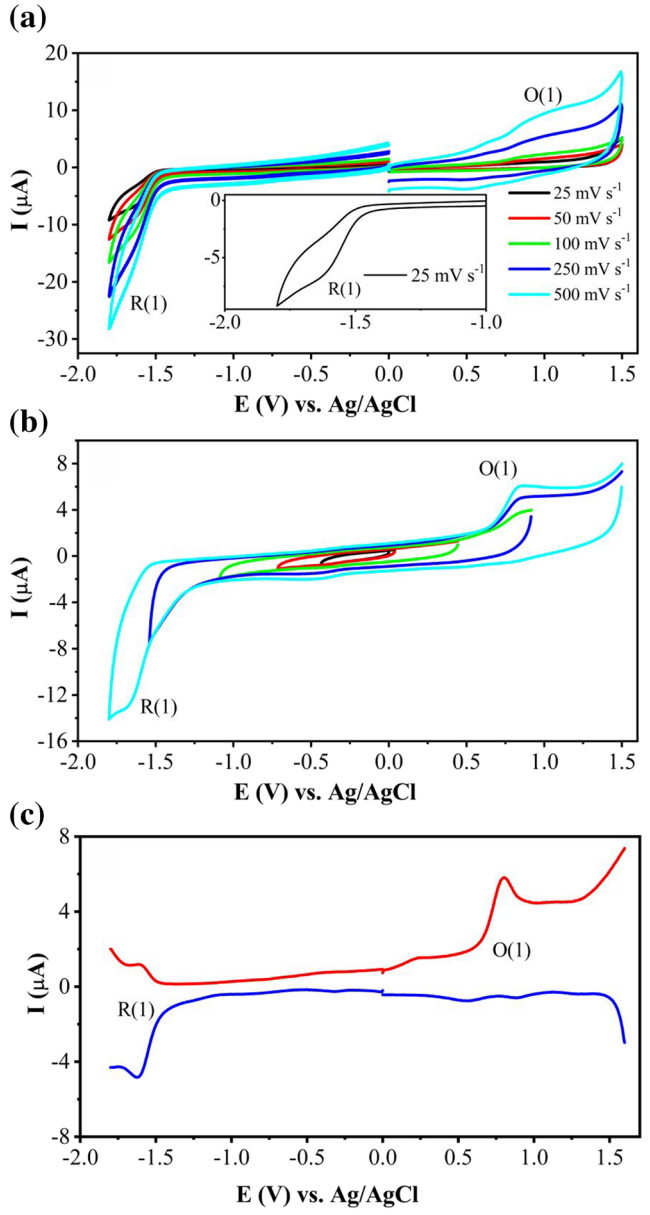

FIGURE 6 Voltammetric responses of **1** on GCE in DCM/TBAP. CV at various scan rates (a); Repetitive CVs recorded with different vertex potentials at 100 mVs^{-1} scan rate (b); SVWs (c).

As shown in Figure 6b and Figure S19b (ESI), altering the vertex potential does not considerably influence the peak characteristics of the complexes. The oxidation processes of both complexes have chemically and electrochemically irreversible characteristics at all scan rates.

The first reduction and oxidation processes are where 1 (Figures 6 and 7) and 2 (Figures S18 and S19, ESI) have significantly different redox behaviours in various electrolytes, according to a comparison of the CV and SWVs. For instance, in DCM/TBAP the first reduction wave *R* (1) at −1.61 V has two electrons transfer character, whereas this wave splits into two couples at −1.58 V and −1.81 V [R(1–1)) and (R(1–2), respectively] in DMSO/TBAP due to the sequential reductions of imine groups of two ligands in **1**.

In DMSO, complex **2** also shows similar voltammetric responses as **1**, with slight potential shifts of the redox processes (Figure S19, ESI). The CPEs of both complexes indicate the proposed number of electron transfer reactions. In addition to the differences in the electron transfer mechanisms, the influence of the succeeding chemical reactions is more dominant in DMSO for both complexes. Due to the oxidation of chemical reaction products, small new waves are observed during the reverse cathodic potential scans. The waves get bigger at fast scan rates and when the vertex potentials become more negative (Figure 7b and Figure S19b, ESI). With respect to those voltammetric findings, the redox mechanism proposed for the redox behaviours of **1** and **2** in DMSO/TBAP is given in Scheme 2.

In situ UV–Vis spectroelectrochemical analysis of **1** and **2** is performed to determine the colour and spectra of the electrogenerated species and to support the proposed mechanisms derived from the voltammetric analysis. In our previous manuscript, we performed a spectroelectrochemical study of the cobalt complex with 2-(2-[pyridine-2-ylmethylene]hydrazinyl)-4-(4-tolyl)-1,-3-thiazole ligand.[43] In that study, the spectral changes associated with the reduction of the cobalt (III) center were presented. Here, the spectral changes of the imine and thiazole based redox reactions are investigated. Complexes **1** and **2** show similar spectroelectrochemical responses. The responses are influenced by electrolyte types due to the coordinating or noncoordinating nature of the solvents for the electrolyte. Figure 8 illustrates the

$$[L-Cd^{2+}-L] - 2e^- \overset{O(1)}{\rightleftharpoons} [L^{1+}-Cd^{2+}-L^{1+}]$$

$$[L-Cd^{2+}-L] + 2e^- \overset{R(1)}{\rightleftharpoons} [L^{1-}-Cd^{2+}-L^{1-}]$$

SCHEME 1 Redox mechanism of **1** and **2** in DCM/TBAP electrolyte.

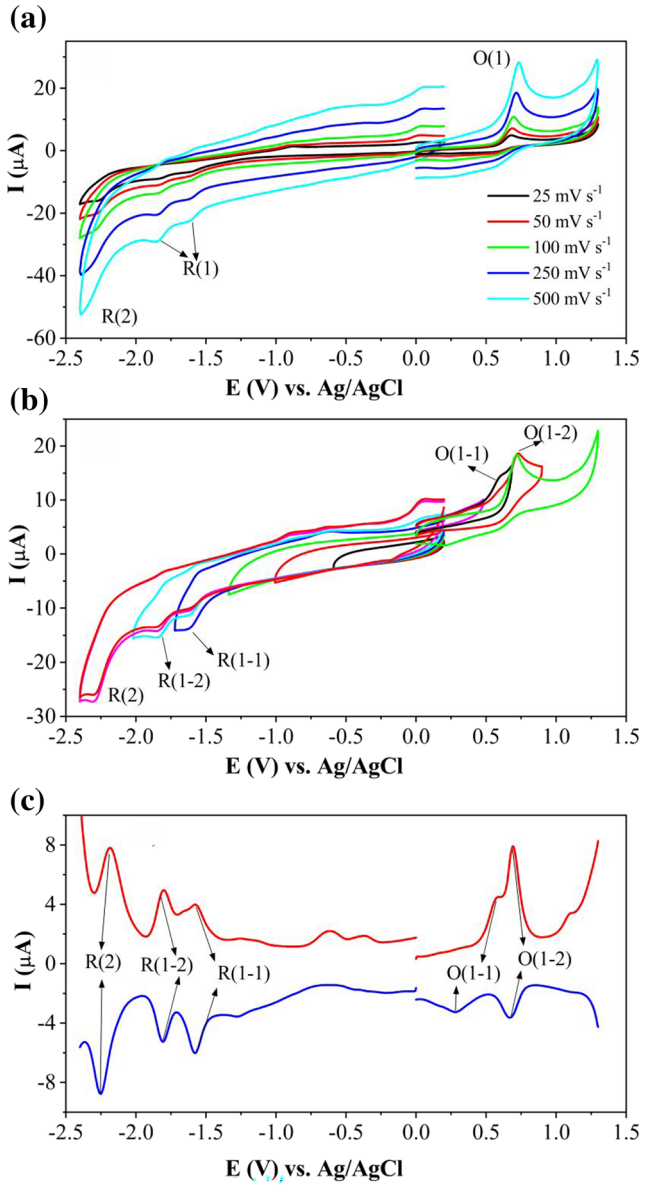

FIGURE 7 Voltammetric responses of **1** on GCE in DMSO/TBAP. CV at various scan rates (a); Repetitive CVs recorded with different vertex potentials at 100 mVs^{-1} scan rate (b); SVWs (c).

in situ spectroelectrochemical behaviour of **1** in DCM/TBAP electrolyte. Under open circuit potential, distinct bands appear at 256, 294, 342, 437, 470 and 498 nm due to the intraligand ($n \rightarrow \pi^*$ and $\pi \rightarrow \pi^*$) transitions. During the *R*(1) process, bands at 256, 342, 470 and 498 nm decrease in absorbance intensity. On the other hand, simultaneous increase in intensity of the bands at 294 and 437 nm was noticed. Moreover, a new charge transfer band is observed at 402 nm.

Although the spectral changes are clearly observed, the intensity of these changes is not so high. Consequently, there is a slight influence on the colour of **1**. The dark orange colour of the neutral **1** (point □; x = 0.489 and y = 0.422) turns to light orange colour (point ◦; x = 0.457 and y = 0.430) as shown in Figure 8d. When the spectral changes are compared with those reported for similar complex,[43] it is clear that the changes are different from those for the metal based reduction process, thus *R*(1) process is assigned to the ligand based electron transfer process. During the oxidation of **1** at 1.0 V (O(1)), two distinct spectral changes are observed. At the beginning of the process, bands at 437, 470 and 498 nm are decreased in intensity. In addition, two new bands are observed at 346 and 395 nm (Figure 8b). Until this point, clear isosbestic points are observed at 303, 336, 415 and 535 nm. These spectral changes are resulted from the 1 e^- reduction of one thiazole group of **1** and the isosbestic points indicate chemical reversibility of the process. Although only one wave is observed for the oxidation of two thiazole groups, spectral changes show that 2 e^- of the O(1) wave occur sequentially, one by one. Figure 8c depicts spectral changes observed during the second electron transfer reaction of **1** at the same applied potential. While the bands at 437, 470 and 498 nm completely disappear, the band at 395 nm continues to increase. Moreover, other bands between 200 and 370 nm decrease in intensity. The intensity of the region at around 650 nm starts to increase and then decreases. Due to the irregular changes of the spectra, isosbestic points continuously oscillate, which indicates chemical irreversibility of the dicationic species produced after the second electron transfer process. These spectral changes are consistent with the spectroelectrochemical responses of thiazoyl-based ligand publish by Caballero et al.[80] Moreover, Krause et al. reported similar spectroelectrochemical responses for the oxidation of thiazolyl-based Pd and Pt complexes.[81] Due to the more dominant spectral changes during the oxidation processes, the dark orange colour ox **1** firstly changes to light orange (point ◇; x = 0.451 and y = 0.400) for the monocationic species and then to light yellow (point ☆; x = 0.373 and y = 0.372) as the colour of the dicationic **1** species, as shown in Figure 8d.

Figure S20 (ESI) illustrates the spectral changes of **2** recorded during the electron transfer reactions in DCM/TBAP. The spectral changes observed during the R(1) of **2** are almost similar to those of **1** (Figure 8). While the band at 486 nm decreases, the bands at 293 and 436 nm increase. Moreover, a new small charge transfer band is observed at 397 nm. These spectral changes cause colour change from dark orange (point □; x = 0.491 and y = 0.419) to light orange (point ◦; x = 0.457 and y = 0.444) as shown in Figure S20D (ESI). All of these spectral changes indicate that R(1) processes of **1** and **2** have the same redox mechanism and result from the 2 e^- reduction of the imine groups of the complexes.

$$[L^{1\pm}Cd^{2+}\text{-}L] - 1e^- \overset{O\,(1\text{-}2)}{\rightleftharpoons} [L^{1+}\text{—}Cd^{2+}\text{-}L^{1+}]$$

$$[L\text{—}Cd^{2+}\text{-}L] - 1e^- \overset{O\,(1\text{-}1)}{\rightleftharpoons} [L^{1+}\text{—}Cd^{2+}\text{-}L]$$

$$[L\text{—}Cd^{2+}\text{-}L] + 1e^- \overset{R\,(1\text{-}1)}{\rightleftharpoons} [L^{1-}\text{—}Cd^{2+}\text{-}L]$$

$$[L^{1-}\text{—}Cd^{2+}\text{-}L] \xrightarrow{\text{succeeding chemical reaction}} \text{Unknown products}$$

$$[L^{1-}\text{—}Cd^{2+}\text{-}L] + 1e^- \overset{R\,(1\text{-}2)}{\rightleftharpoons} [L^{1-}\text{—}Cd^{2+}\text{-}L^{1-}]$$

$$[L^{1-}\text{—}Cd^{2+}\text{-}L^{1-}] \xrightarrow{\text{succeeding chemical reaction}} \text{Unknown products}$$

$$[L^{1-}\text{—}Cd^{2+}\text{-}L^{1-}] + 2e^- \overset{R\,(2)}{\rightleftharpoons} [L^{2-}\text{—}Cd^{2+}\text{-}L^{2-}]$$

SCHEME 2 Redox mechanism of **1** and **2** in DMSO/TBAP electrolyte.

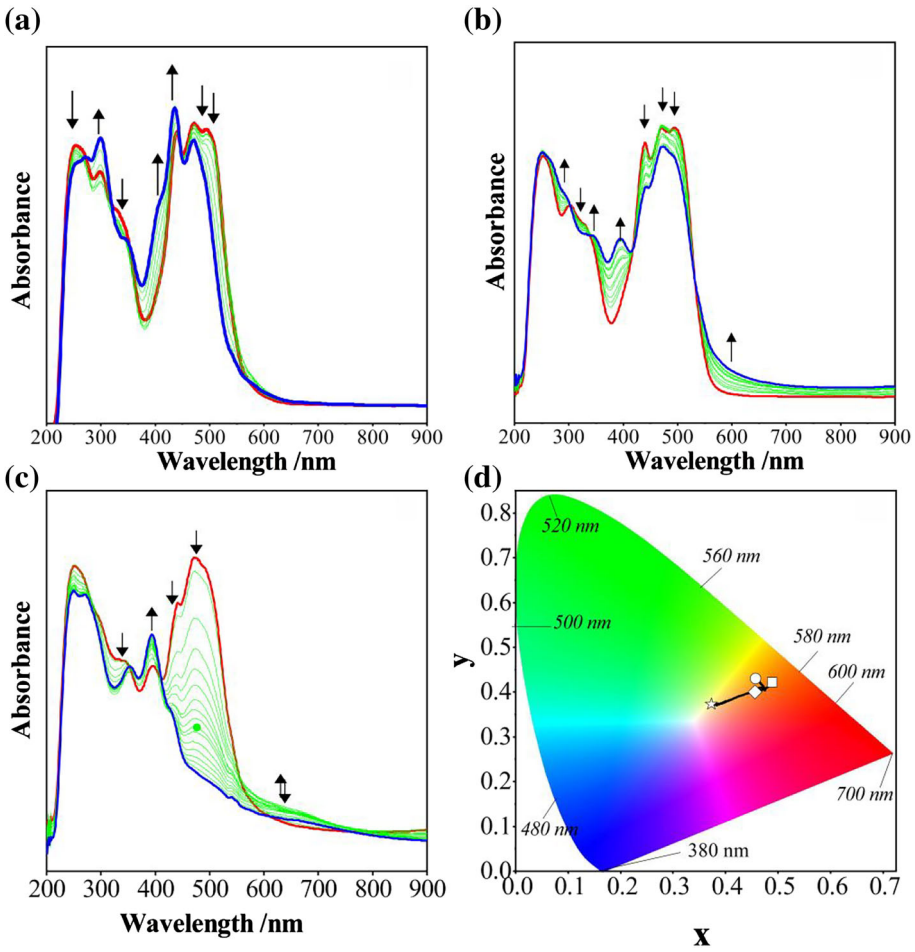

FIGURE 8 UV–Vis spectral changes of **1** recorded during *in situ* spectroelectrochemical measurements at applied potentials: (a) $E_{app} = -1.75$ V, (b and c) $E_{app} = 1.00$ V in DCM/TBAP electrolyte system (changes of the spectrum during the redox reactions were marked with the arrows); (d) colour of the species (Neutral: □; R (1): ◦; O(1, frontier): ◇; O(1, later): ☆).

Similarly, under the applied potential of 1.0 V, two distinct spectral changes were observed, due to the sequential electron transfer reactions during the O(1) wave of **2**. Complex **2** showed very similar spectral changes to those observed for **1** during the first $1e^-$ transfer, giving monocationic species. During this process, while the bands at 436 and 486 nm almost disappear, a new band is observed at 387 nm (Figure S20B, ESI). Clear isosbestic

points are observed at 404 and 557 nm, which indicates chemical reversibility of the monocationic species of **2**. These spectral changes caused the colour change from dark orange to yellow (Figure S20, ESI). During the reduction of monocation to the dication of **2**, completely different spectral changes are observed than those of **1** as shown in Figure S20C (ESI). Two new bands are enhanced at 434 and 590 nm with an isosbestic point at 376 nm (Figure S20C, ESI), which indicates chemical reversibility of the dicationic form of **2**. These spectral changes caused colour changes from dark orange to yellow (point ◇; x = 0.381 and y = 0.381) and then green (point ☆; x = 0.345 and y = 0.420) after the oxidation processes as illustrated in Figure S20D (ESI).

In situ spectroelectrochemical measurements of **1** and **2** are also measured in DMSO/TBAP electrolyte to support the proposed mechanism performed with voltammetric analyses. Details are given in ESI.

Significant changes in the optical behaviours of **1** and **2** in the UV–Vis region of the light spectrum observed during redox processes indicate the usability of these materials in different electrochromic applications.

3.7 | Antioxidant capacity (AOC)

To the best of our knowledge, AOC studies of CCs with THs ligands have not been published up to now. Herein we report the results of in vitro AOC of **1** and **2**, obtained from two radical scavenger assays (ABTS and ORAC) and one reducing capacity assay (CERAC) (Table 4). For comparison, previously published results from our group relating to AOC of HLS^2 and HLS^3 in ABTS and ORAC assays are also presented in Table 4.[40,43] Data regarding HLS^2 and HLS^3 activities in the CERAC assay was obtained in this study.

As can be seen from these data, the AOC of **1** and **2** is notably better (lower IC_{50}, higher TE values) than for corresponding ligands. Specifically, the most prominent differences (%) were observed in the ORAC assay. In general, compounds' ranges of antioxidant activity of **1** and **2** are quite similar (Table 4). Both, **1** and **2** exhibit comparable or even more pronounced antioxidant potential than standard antioxidants (Trolox and ascorbic acid/Vitamin C) in ABTS and ORAC assays.

TABLE 4 Antioxidant capacity of investigated ligands (HLS^2 and HLS^3) and their Cd(II) complexes (**1** and **2**)

Test/Units Labels	ABTS	CERAC	ORAC
	IC_{50} (μM)[a]		TE[a]
HLS^2	214 ± 7	491 ± 15	0.71 ± 0.031
HLS^3	235 ± 8	547 ± 20	0.68 ± 0.029
1	194 ± 5	364 ± 14	0.97 ± 0.021
2	220 ± 5	376 ± 18	0.94 ± 0.025
Trolox	145 ± 4	292 ± 11	1
Ascorbic acid	219 ± 6	261 ± 15	0.93 ± 0.040

[a]Values are means of three replicates ± standard deviation.

3.8 | Antimicrobial activity

The antimicrobial activity of the HLS^2 and HLS^3 ligands, their Cd complexes **1** and **2**, Cd(II)-salt used in synthesis and Erythromycin was examined against five Gram-negative bacteria: *E. Coli*, *P. aeruginosa*, *P. hauseri*, *K. pneumoniae* and *S. enterica*, as well as four Gram-positive bacteria: *S. aureus*, *M. luteus ATCC 4698*, *M. luteus ATCC 10240* and *C. Sporogenes* (Table 5). The antifungal activity of the investigated compounds was examined against *S. cerevisiae*, *A. brasiliensis*, and *C. albicans* (Table S5, ESI).

The synergetic effect of complexation of Cd(II) with HLS^2 and HLS^3 ligands on antibacterial activity is observed since **1** and **2** were far more active compared to the corresponding free ligands and cadmium-perchlorate. Both complexes showed micromolar activity, while **1** was more active on all strains. Complex **1** was more active on all bacterial strains except *P. hauseri* and *K. pneumoniae* compared to erythromycin. Also, **2** showed better activity than antibiotic control against two Gram-negative bacteria, *S. aureus* and *C. sporogenes*. On the other hand, both complexes showed significantly lower antifungal activity compared to Amphotericin B (Table S5, ESI), despite the fact that there is a synergistic effect between Cd(II) and TH ligands.

3.9 | Docking to DNA

To determine the binding modes of investigated Cd(II) complexes to DNA, which refer to possible mechanisms of biological activity of the complexes, molecular docking was performed. The results of the docking study revealed three binding sites for both complexes to DNA. Binding in minor groove of DNA is slightly stronger than binding in the major groove, in the case of both complexes. In the case of **1**, the first binding site (BS1, −3.64 kcal/mol) is located in the G ≡ C rich region of the minor groove (Figure 9). The second binding site (BS2, −3.30 kcal/mol) is also located in the minor groove but in the transition region, between G ≡ C rich and A = T rich regions. Only the third binding site is located in the major groove (BS3, −3.25 kcal/mol). As in the case of **1**,

TABLE 5 Antimicrobial effects of investigated compounds

MIC (mM)									
Compound	***E. coli***	***P. aeruginosa***	***P. hauseri***	***K. pneumoniae***	***S. enterica***	***S. aureus***	***M. luteus* ATCC 4698**	***M. luteus* ATCC 10240**	***C. sporogenes***
1	0.021	0.021	0.043	0.043	0.011	0.011	0.011	0.021	0.021
2	0.045	0.090	0.045	0.045	0.045	0.045	0.045	0.045	0.045
HLS[2]	8.055	4.027	8.055	8.055	8.055	8.055	8.055	8.055	8.055
HLS[3]	8.492	4.246	8.492	8.492	8.492	8.492	8.492	8.492	8.492
Cd-salt	0.126	0.504	0.504	0.504	0.504	1.009	0.064	2.017	2.017
Erythromycin	0.038	0.076	0.038	0.038	0.038	0.076	0.019	0.038	0.076

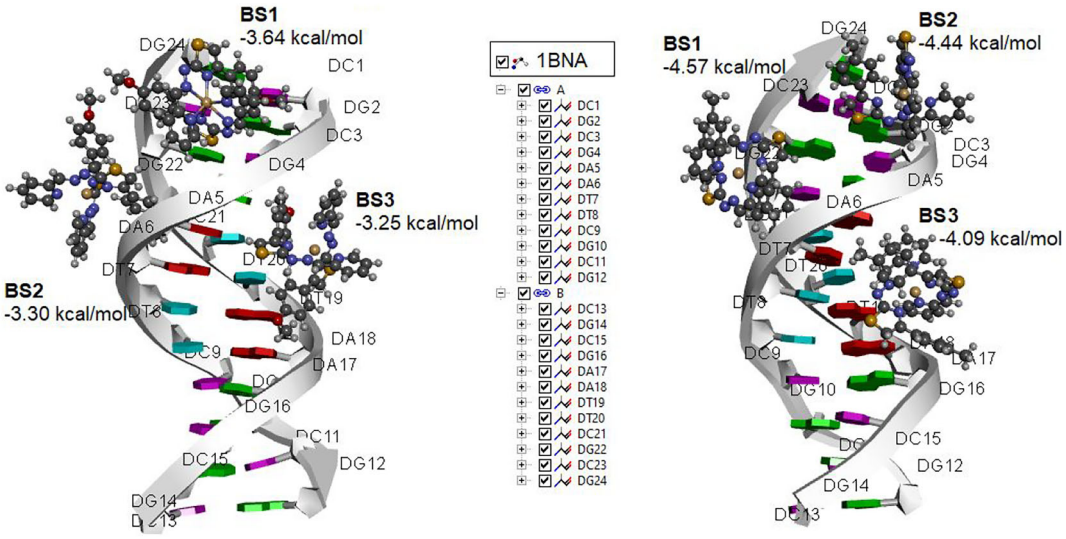

FIGURE 9 The most stable binding modes of **1** (left) and **2** (right) to DNA, as assessed by molecular docking.

the first binding site of **2** is located in minor groove (BS1, −4.57 kcal/mol), but in the transition region (Figure 9). The second binding site is located in the G ≡ C rich region of minor groove (BS2, −4.44 kcal/mol), while the third binding site is located in the major groove (BS3, −4.09 kcal/mol).

In BS1, **1** interacts with three nucleotides from the G ≡ C rich region. All three subunits of nucleotides (nucleobase, five-carbon sugar subunit and phosphate backbone) are involved in the interactions. Investigated complexes do not have a donor group for classical hydrogen bonding but only CH groups. The acceptor abilities of **1** are based on O atoms of methoxy groups and π-systems of aromatic, heterocyclic and chelated rings. The strongest interactions of **1** in BS1 include N–H groups of nucleobase (N–H···O and N–H···π interactions). With sugar subunits, the complex forms mainly C–H···O interactions, in which the complex is a donor of the C–H group. It forms only one C–H···O interaction with the phosphate backbone, which is weak in strength. In BS2, the classical hydrogen bonds were not observed; hence, it is a possible reason for lower binding energy, compared to BS1. Additionally, **1** forms slightly more interactions with the sugar subunit (mainly C–H···π interactions) than with nucleobases (mainly C–H···O interactions). With the phosphate backbone, **1** forms only one C–H···O interaction, as in the case of BS1. Despite the fact that **1** in BS3 interacts with the same number of nucleotides as in the case of BS1 and BS2, it showed lower affinity for binding in major groove. The possible reason is the lower number of interactions with these nucleotides. There is no classical hydrogen bond with DNA in BS3. The interactions with nucleobases are the most represented (C–H···O, C–H···N, and C–H···π interactions). With the phosphate backbone, **1** forms only one C–H···O interaction, whereas it does not interact with the sugar subunit.

Although **2** does not contain O atoms, it has a slightly higher affinity for binding to DNA (with higher binding energies) than **1**. In BS1, **2** mainly forms interactions with

sugar subunits (C–H···O and C–H···π interactions). It also forms multiple C–H···π interactions with nucleobases and C–H···O interactions with the phosphate backbone. Hence, these interactions have slightly shorter bond lengths than in the previous cases; hence, that is a possible explanation for the higher binding energies of **2** to DNA, compared to **1**. In BS2, **2** forms a similar number of interactions with nucleobases (C–H···O and C–H···N interactions) and with sugar subunits (C–H···O and C–H···π interactions). In addition, the **2** forms only two C–H···O interactions with phosphate backbone. BS3 is located in the major groove, which allows an easier approach of complexes to nucleobases. Therefore, **2** in BS3 mainly forms the interactions with nucleobases (mainly C–H···N interactions) and only two C–H···O interactions with the phosphate backbone. At this binding site, the complex does not form interactions with the sugar subunit.

4 | CONCLUSION

In this study, we performed synthesis and characterization of the first Cd(II) complexes (**1** and **2**) with the anionic form of pyridine-based THs ligands HLS^2 and HLS^3. Based on the results of single-crystal XRD, THs ligands are NNN tridentately coordinated to Cd(II) in an octahedral environment, forming neutral complexes of general formula $[Cd(LS^n)]$ (n = 2 for **1** and n = 3 for **2**). The most dominant interactions in the crystal packings are C···H, S···H and N···H interactions. In the case of **1**, a significant amount of O···H interactions are also identified as a consequence of the existence of oxygen atoms from the methoxy group. Since hydrogen bonds are stronger than C···H interactions, they are recognized as being responsible for the solid-state structures of **1** and **2**.

Both complexes showed a slight mass loss upon heating in the range from 60 to 200 °C in argon and air. Because of the low amounts of the evaporated fragments and the wide temperature range of evaporation, the evaporated products in this temperature range were not detectable by the coupled TG-MS analysis. The decomposition processes of the compounds become intensive at around 220 °C. Above this temperature, the fragmentation of the ligands was observed and the corresponding fragments were detected by coupled TG-MS measurements.

The values of the first gradual stability constants (log K_{11}) for **1** and **2** are lower than in the case of their counterparts obtained from neutral ligands and Cd(II). On the other hand, overall higher log β_{12} values and the second gradual stability constants (log K_{12}) for both studied complexes are higher compared with their mentioned counterparts. This indicates that deprotonation of the ligands favours the presence of a stable complex form with a desired 1:2 stoichiometry (ML_2) in solution.

Complexes **1** and **2** undergo imine-based irreversible reduction and thiazole-based oxidation processes. While only one wave has 2 e^--transfer-characters for two imine groups and one wave 2 e^--transfer-characters for two thiazole groups of the complexes in DCM/TBAP, these waves were split into two waves having 1e^--transfer for each imine and thiazolyl groups of the ligands in DMSO/TBAP. While spectral changes observed during the reduction process were not predominant, distinct spectral and colour changes were observed during the oxidation processes, which indicates their possible functionality for the anionic electrochromic applications.

The antioxidant capacity of Cd(II) complexes with THs ligands has not been investigated up to this study to the best of our knowledge. Our results revealed that the complexation of pyridine-based THs with Cd(II) results in complexes that possess higher AOC than the corresponding ligands in ABTS, CERAC and ORAC assays.

A significant synergistic effect of HLS^2 and HLS^3 complexation with Cd(II) on antimicrobial activity was also observed. Results obtained on bacteria are more promising since observed activities are significantly higher when compared with standard antibiotics Erythromycin. It is important to note that activities obtained against bacteria do not originate from Cd(II) itself, since MIC values for Cd(II) salt are higher than values for the complexes on all five Gram-positive and four Gram-negative bacteria. The results of the molecular docking study indicate that the possible mechanism of biological activity of the complexes is related to their binding to the minor groove of DNA. Although binding to the major groove is possible on the basis of the docking study, it has a lower affinity. Interactions with the phosphate backbone have been observed (only C–H···O interactions). However, the C–H···O interactions are not strong enough to cause the bending of the DNA structure, which was observed when the positively charged complexes are bound to the phosphate backbone.[82] Despite the numerous aromatic and chelated rings, intercalation should not be expected due to steric reasons.

Due to increase in resistance of bacteria to existing antibiotics, we hope that our results will draw the attention of the scientific community to the antimicrobial activity of TH ligands' complexes with various metals, including cadmium.

ACKNOWLEDGEMENTS

The work was supported by the Ministry of Education, Science and Technological Development of the Republic of Serbia under Grants 451-03-68/2022-14/200168,

451-03-68/2022-14/200116, 451-03-68/2022-14/200125 and 451-03-68/2022-14/200026. The authors Özlem Uğuz and Atıf Koca would like to thank to Turkish Academy of Sciences (TÜBA) for the financial support.

AUTHOR CONTRIBUTIONS

Sanja B. Kokanov: Investigation. **Nenad R. Filipović:** Conceptualization; formal analysis; supervision; writing-original draft. **Aleksandar Višnjevac:** Formal analysis; methodology; visualization. **Milan Nikolić:** Formal analysis; methodology. **Irena Novaković:** Formal analysis; methodology. **Goran Janjić:** Methodology; software; visualization. **Berta Barta Holló:** Formal analysis; methodology; visualization. **Sandra Ramotowska:** Formal analysis; investigation; visualization. **Paulina Nowicka:** Investigation; methodology; visualization. **Mariusz Makowski:** Resources; supervision; writing-review and editing. **Özlem Uğuz:** Formal analysis; investigation; visualization. **Atıf Koca:** Formal analysis; investigation; supervision; writing-review and editing. **Tamara R. Todorović:** Conceptualization; formal analysis; resources; supervision; writing-review and editing.

CONFLICTS OF INTEREST

No potential conflict of interest was reported by the authors.

DATA AVAILABILITY STATEMENT

Data available on request from the authors.

ORCID

Sanja B. Kokanov https://orcid.org/0000-0001-6817-7409
Nenad R. Filipović https://orcid.org/0000-0003-2982-5324
Aleksandar Višnjevac https://orcid.org/0000-0002-4382-6908
Milan Nikolić https://orcid.org/0000-0003-0932-889X
Irena Novaković https://orcid.org/0000-0001-9881-1204
Goran Janjić https://orcid.org/0000-0002-4138-2637
Berta Barta Holló https://orcid.org/0000-0002-5786-442X
Sandra Ramotowska https://orcid.org/0000-0003-1212-0395
Paulina Nowicka https://orcid.org/0000-0002-6656-8673
Mariusz Makowski https://orcid.org/0000-0002-7342-722X
Özlem Uğuz https://orcid.org/0000-0001-7895-2296
Atıf Koca https://orcid.org/0000-0003-0141-5817
Tamara R. Todorović https://orcid.org/0000-0002-7740-3639

REFERENCES

[1] M. Schmid, S. Zimmermann, H. F. Krug, B. Sures, *Environ. Int.* **2007**, *33*, 385.
[2] S. B. Marković, A. V. Natalia Maciejewska, M. Olszewski, A. Puerta, J. M. Padrón, I. Novaković, S. Kojić, H. S. Fernandes, S. F. Sousa, S. Ramotowska, A. Chylewska, M. Makowski, T. R. Todorović, N. R. Filipović, *Eur. J. Med. Chem.* **2022**, *238*, 11449.
[3] Z. Zhang, C. Bi, D. Buac, Y. Fan, X. Zhang, J. Zuo, P. Zhang, N. Zhang, L. Dong, Q. P. Dou, *J. Inorg. Biochem.* **2013**, *123*, 1.
[4] S. Bjelogrlić, T. R. Todorović, I. Cvijetić, M. V. Rodić, M. Vujčić, S. Marković, J. Araškov, B. Janović, F. Emhemmed, C. D. Muller, N. R. Filipović, *J. Inorg. Biochem.* **2019**, *190*, 45.
[5] A. Frei, *Antibiotics* **2020**, *9*, 90.
[6] S. Nasiri Sovari, F. Zobi, *Chemistry (Easton)* **2020**, *2*, 418.
[7] E. M. Abdalla, L. H. Abdel Rahman, A. A. Abdelhamid, M. R. Shehata, A. A. Alothman, A. Nafady, *Appl. Organomet. Chem.* **2020**, *34*, e5912.
[8] P. A. Khalaf-Alla, *Appl. Organomet. Chem.* **2020**, *34*, e5628.
[9] S. S. Hassan, P. A. Khalf-Alla, *Appl. Organomet. Chem.* **2020**, *34*, e5432.
[10] M. Gaber, K. El-Baradie, N. El-Wakiel, S. Hafez, *Appl. Organomet. Chem.* **2020**, *34*, e5348.
[11] W. H. Mahmoud, G. G. Mohamed, A. M. Refat, *Appl. Organomet. Chem.* **2017**, *31*, e3753.
[12] W. H. Mahmoud, F. N. Sayed, G. G. Mohamed, *Appl. Organomet. Chem.* **2016**, *30*, 959.
[13] S. X. Cui, Q. Z. Yin, J. H. Yu, J. Jiang, Y. C. Zou, *Russ. J. Inorg. Chem.* **2020**, *65*, 874.
[14] Q.-X. Yao, Z.-F. Ju, X.-H. Jin, J. Zhang, *Inorg. Chem.* **2009**, *48*, 1266.
[15] D.-D. Yang, H.-W. Zheng, Q.-F. Liang, M. Wu, J.-B. Li, R. Duan, F.-B. Jiang, X.-J. Zheng, *Inorg. Chem.* **2021**, *60*, 13500.
[16] M.-S. Wang, G.-C. Guo, W. Q. Zou, W.-W. Zhou, Z.-J. Zhang, G. Xu, J.-S. Huang, *Angew. Chem., Int. Ed.* **2008**, *47*, 3565.
[17] H. Y. Wang, S. Liu, C. Fu, H. Zhang, *CrystEngComm* **2019**, *21*, 1635.
[18] J. J. Liu, J. Li, *Dyes Pigm.* **2019**, *170*, 107565.
[19] N. Kundu, S. M. T. Abtab, S. Kundu, A. Endo, S. J. Teat, M. Chaudhury, *Inorg. Chem.* **2012**, *51*, 2652.
[20] M. J. Hurlock, M. F. Lare, Q. Zhang, *Inorg. Chem.* **2021**, *60*, 2503.
[21] J. W. Shin, J. M. Bae, C. Kim, K. S. Min, *Inorg. Chem.* **2013**, *52*, 2265.
[22] R. Pandey, A. Kumar, Q. Xu, D. S. Pandey, *Dalton Trans.* **2020**, *49*, 542.
[23] C. H. Liu, Q. L. Guan, X. D. Yang, F. Y. Bai, L. X. Sun, Y. H. Xing, *Inorg. Chem.* **2020**, *59*, 8081.
[24] W.-H. Huang, J. Ren, Y.-H. Yang, X.-M. Li, Q. Wang, N. Jiang, J.-Q. Yu, F. Wang, J. Zhang, *Inorg. Chem.* **2019**, *58*, 1481.
[25] Z.-K. Wang, M.-M. Sheng, S.-S. Qin, H.-T. Shi, M. Strømme, Q. F. Zhang, C. Xu, *Inorg. Chem.* **2020**, *59*, 2121.
[26] W. Meng, Z. Xu, J. Ding, D. Wu, X. Han, H. Hou, Y. Fan, *Cryst. Growth des.* **2014**, *14*, 730.
[27] C. L. Yadav, Anamika, G. Rajput, K. Kumar, M. G. B. Drew, N. Singh, *Inorg. Chem.* **2020**, *59*, 11417.
[28] R. Pandey, D. Singh, N. Thakur, K. K. Raj, *ACS Omega* **2021**, *6*, 13240.

[29] V. Gupta, S. K. Mandal, *Inorg. Chem.* **2019**, *58*, 3219.
[30] Y. Rachuri, J. F. Kurisingal, R. K. Chitumalla, S. Vuppala, Y. Gu, J. Jang, Y. Choe, E. Suresh, D.-W. Park, *Inorg. Chem.* **2019**, *58*, 11389.
[31] K. Roztocki, M. Szufla, V. Bon, I. Senkovska, S. Kaskel, D. Matoga, *Inorg. Chem.* **2020**, *59*, 10717.
[32] C. E. Morrison, F. Wang, N. P. Rath, B. M. Wieliczka, R. A. Loomis, W. E. Buhro, *Inorg. Chem.* **2017**, *56*, 12920.
[33] M. J. Foody, M. S. Weimer, H. Bhandari, A. S. Hock, *Inorg. Chem.* **2021**, *60*, 6191.
[34] C. Huang, G. Lu, Y. Zhang, K. Zhu, S. Cui, W. Chen, Z. Wu, M. Qiu, L. Mi, *Inorg. Chem.* **2021**, *60*, 550.
[35] L. J. Daumann, L. R. Gahan, P. Comba, G. Schenk, *Inorg. Chem.* **2012**, *51*, 7669.
[36] A. A. Majeed, M. M. H. Khalil, A. Fetoh, A. A. Abdel Aziz, G. M. Abu El-Reash, *Appl. Organomet. Chem.* **2020**, *35*, e6037.
[37] K. Abou-Melha, *J. Mol. Struct.* **2021**, *1223*, 128949.
[38] T. A. Yousef, G. M. Abu El-Reash, M. Al-Jahdali, E.-B. R. El-Rakhawy, *Spectrochim. Acta - Part a Mol. Biomol. Spectrosc.* **2014**, *129*, 163.
[39] R. Manikandan, N. Chitrapriya, Y. J. Jang, P. Viswanathamurthi, *RSC Adv.* **2013**, *3*, 11647.
[40] J. B. Araškov, M. Nikolić, S. Armaković, S. Armaković, M. Rodić, A. Višnjevac, J. M. Padrón, T. R. Todorović, N. R. Filipović, *J. Mol. Struct.* **2021**, *1240*, 130512.
[41] H. Elshaflu, S. Bjelogrlić, C. D. Muller, T. R. Todorović, M. Rodić, A. Marinković, N. R. Filipović, *J. Coord. Chem.* **2016**, *69*, 3354.
[42] A. Borges, M. Simões, T. R. Todorović, N. R. Filipović, A. T. Garcia-Sosa, *Molecules* **2018**, *23*.
[43] N. R. Filipović, H. Elshaflu, S. Grubišić, L. S. Jovanović, M. Rodić, I. Novaković, A. Malešević, I. S. Djordjević, H. Li, N. Šojić, A. Marinković, T. R. Todorović, *Dalton Trans.* **2017**, *46*, 2910.
[44] CrysAlis CCD, *Oxford Diffraction Ltd., Version 1.171.32.29*.
[45] M. C. Burla, R. Caliandro, B. Carrozzini, G. L. Cascarano, C. Cuocci, C. Giacovazzo, M. Mallamo, A. Mazzone, G. Polidori, *J. Appl. Crystallogr.* **2015**, *48*, 306.
[46] G. M. Sheldrick, *Acta Crystallogr. Sect. C Struct. Chem.* **2015**, *71*, 3.
[47] C. F. Macrae, I. J. Bruno, J. A. Chisholm, P. R. Edgington, P. McCabe, E. Pidcock, L. Rodriguez-Monge, R. Taylor, J. Van De Streek, P. A. Wood, *J. Appl. Crystallogr.* **2008**, *41*, 466.
[48] L. J. Farrugia, *J. Appl. Crystallogr.* **1999**, *32*, 837.
[49] A. L. Spek, *Acta Crystallogr. Sect. D Biol. Crystallogr.* **2009**, *65*, 148.
[50] M. Guin, S. Khanna, S. B. Elavarasi, P. Sarkar, *J. Chem. Sci.* **2020**, *132*, 1.
[51] J. J. McKinnon, M. A. Spackman, A. S. Mitchell, *Acta Crystall. Sect. A* **2004**, *60*, 627.
[52] J. J. McKinnon, D. Jayatilaka, M. A. Spackman, *Chem. Commun.* **2007**, *37*, 3814.
[53] M. J. Frisch, G. W. Trucks, H. B. Schlegel, G. E. Scuseria, M. A. Robb, J. R. Cheeseman, G. Scalmani, V. Barone, G. A. Petersson, H. Nakatsuji, X. Li, M. Caricato, A. Marenich, J. Bloino, B. G. Janesko, R. Gomperts, B. Mennucci, H. P. Hratchian, J. V. Ortiz, A. F. Izmaylov, J. L. Sonnenberg, D. Williams-Young, F. Ding, F. Lipparini, F. Egidi, J. Goings, B. Peng, A. Petrone, T. Henderson, D. Ranasinghe, V. G. Zakrzewski, J. Gao, N. Rega, G. Zheng, W. Liang, M. Hada, M. Ehara, K. Toyota, R. Fukuda, J. Hasegawa, M. Ishida, T. Nakajima, Y. Honda, O. Kitao, H. Nakai, T. Vreven, K. Throssell, J. A. Montgomery Jr., J. E. Peralta, F. Ogliaro, M. Bearpark, J. J. Heyd, E. Brothers, K. N. Kudin, V. N. Staroverov, T. Keith, R. Kobayashi, J. Normand, K. Raghavachari, A. Rendell, J. C. Burant, S. S. Iyengar, J. Tomasi, M. Cossi, J. M. Millam, M. Klene, C. Adamo, R. Cammi, J. W. Ochterski, R. L. Martin, K. Morokuma, O. Farkas, J. B. Foresman, D. J. Fox, *Gaussian 09, Revision A.02*, Gaussian, Inc., Wallingford CT **2009**.
[54] H. R. Drew, R. M. Wing, T. Takano, C. Broka, S. Tanaka, K. Itakura, R. E. Dickerson, *Proc. Natl. Acad. Sci. U. S. a.* **1981**, *78*, 2179.
[55] G. M. Morris, R. Huey, W. Lindstrom, M. F. Sanner, R. K. Belew, D. S. Goodsell, A. J. Olson, *J. Comput. Chem.* **2009**, *30*, 2785.
[56] *Discovery Studio Modeling Environment*, Dassault Systèmes BIOVIA, San Diego, CA, USA **2017**.
[57] J. Kostrowicki, A. Liwo, *Talanta* **1990**, *37*, 645.
[58] J. Kostrowicki, A. Liwo, *Comput. Chem.* **1987**, *11*, 195.
[59] A. Wcisło, A. Cirocka, D. Zarzeczańska, P. Niedziałkowski, S. Nakonieczna, T. Ossowski, *Spectrochim. Acta Part a Mol. Biomol. Spectrosc.* **2015**, *137*, 976.
[60] T. Ossowski, H. Sulowska, T. Karbowiak, D. Zarzeczanska, B. Gierczyk, G. Schroeder, *Cent. Eur. J. Cent. Eur. J. Chem.* **2006**, *4*, 13.
[61] D. Akyüz, A. Koca, *Sens. Actuators, B* **2019**, *283*, 848.
[62] S. Duman, I. Kizilcikli, A. Koca, M. Akkurt, B. Ülküseven, *Polyhedron* **2010**, *29*, 2924.
[63] A. Augusti Boligon, M. Mansur Machado, M. Linde Athayde, *Tech. Eval. Antioxid. Act. Med. Chem.* **2014**, *4*, 517.
[64] B. Ou, M. Hampsch-Woodill, R. L. Prior, *J. Agric. Food Chem.* **2001**, *49*, 4619.
[65] D. Ozyurt, B. Demirata, R. Apak, *J. Food Compos. Anal.* **2010**, *23*, 282.
[66] National Committee for Clinical Laboratory Standards, *Approval Standard Document M7-A5*, Villanova, Pa, USA **2000**.
[67] A. Sartoratto, A. L. M. Machado, C. Delarmelina, G. M. Figueira, M. C. T. Duarte, V. L. G. Rehder, *Brazilian J. Microbiol.* **2004**, *35*, 275.
[68] A. M. Lazić, I. S. Đorđević, L. D. Radovanović, D. M. Popović, J. R. Rogan, G. V. Janjić, N. P. Trišović, *ChemPlusChem* **2020**, *85*, 1220.
[69] S. Harisha, J. Keshavayya, B. E. Kumara Swamy, C. C. Viswanath, *Dyes Pigm.* **2017**, *136*, 742.
[70] H. Maqbool, S. D. Ganesh, U. Chandra, B. E. Kumaraswamy, V. K. Pai, *Res. J. Chem. Sci.* **2013**, *3*, 44.
[71] N. Menek, O. Çakir, H. Kocaokutgen, *Microchim. Acta* **1996**, *122*, 203.
[72] N. Raju, A. Ramachandraiah, *E-Journal Chem.* **2010**, *7*, 583.
[73] M. Özkütük, E. Ipek, B. Aydiner, S. Mamaş, Z. Seferoḷlu, *J. Mol. Struct.* **2016**, *1108*, 521.
[74] J. Palion-Gazda, B. Machura, T. Klemens, A. Szlapa-Kula, S. Krompiec, M. Siwy, H. Janeczek, E. Schab-Balcerzak, J. Grzelak, S. Maćkowski, *Dyes Pigm.* **2019**, *166*, 283.
[75] K. Godugu, T. R. Gundala, R. Bodapati, V. D. S. Yadala, S. S. Loka, C. G. R. Nallagondu, *New J. Chem.* **2020**, *44*, 7007.

[76] Ö. Göktuğ, D. Akyüz, A. Koca, M. Kasım Şener, *J. Coord. Chem.* **2017**, *70*, 2052.
[77] S. Y. Ebrahimipour, I. Sheikhshoaie, J. Castro, W. Haase, M. Mohamadi, S. Foro, M. Sheikhshoaie, S. Esmaeili-Mahani, *Inorg. Chim. Acta* **2015**, *430*, 245.
[78] I. Sheikhshoaie, S. Y. Ebrahimipour, M. Sheikhshoaie, M. Mohamadi, M. Abbasnejad, H. A. Rudbari, G. Bruno, *J. Chem. Sci.* **2015**, *127*, 2193.
[79] S. Biswas, A. K. Pramanik, T. K. Mondal, *J. Mol. Struct.* **2015**, *1088*, 28.
[80] A. Caballero, V. Lloveras, D. Curiel, A. Tárraga, A. Espinosa, R. García, J. Vidal-Gancedo, C. Rovira, K. Wurst, P. Molina, J. Veciana, *Inorg. Chem.* **2007**, *46*, 825.
[81] M. Krause, R. von der Stück, D. Brünink, S. Buss, N. L. Doltsinis, C. A. Strassert, A. Klein, *Inorg. Chim. Acta* **2021**, 518.
[82] A. A. Franich, I. S. Đorđević, M. D. Živković, S. Rajković, G. V. Janjić, M. I. Djuran, *J. Biol. Inorg. Chem.* **2021**, *27*, 65.

SUPPORTING INFORMATION

Additional supporting information can be found online in the Supporting Information section at the end of this article.

How to cite this article: S. B. Kokanov, N. R. Filipović, A. Višnjevac, M. Nikolić, I. Novaković, G. Janjić, B. B. Holló, S. Ramotowska, P. Nowicka, M. Makowski, Ö. Uğuz, A. Koca, T. R. Todorović, *Appl Organomet Chem* **2023**, *37*(1), e6942. https://doi.org/10.1002/aoc.6942